MULTIPARTICLE EVENTS WITH IDENTIFIED FINAL STATE PROTONS RESULTING FROM pp INTERACTIONS AT 28.5 GeV/c

by

Blair Culver Stringfellow

Dissertation submitted to the Graduate Faculty of the
Virginia Polytechnic Institute and State University
in partial fulfillment of the requirements for the degree of

DOCTOR OF PHILOSOPHY

in

Physics

APPROVED:

W. P. Trower, Chairman

J. A. Jacobs

M. C. Li

R. J. Onega

J. R. Long

September, 1973

Blacksburg, Virginia

ACKNOWLEDGMENTS

I am most grateful to the many collaborators on this experiment, both here at V.P.I. and at Brookhaven. I have benefited greatly by my association with all of them. I would especially like to thank Dr. P. Schübelin, Dr. F. Turkot, Mr. R. Rothe and Mr. E. Bihn at Brookhaven for their interest in my work and assistance during my stay there. Mr. D.R. Gilbert and Mr. W.N. Schreiner, with whom I have had many hours of helpful discussion, have also provided invaluable computer programming assistance for which I am grateful. Mrs. M.A. Stevens has done all the technical work related to the preparation of this thesis. I am very thankful for her interest, care and hard work. I would especially like to thank Dr. J. Ficenec for his patience and encouragement, as well as his many meaningful suggestions during the preparation of this work.

Finally to my thesis advisor, Dr. W.P. Trower, I wish to express my thanks for his guidance and for providing me with the opportunity to participate in this experiment. His ideas and suggestions have been invaluable in preparing this thesis.

TABLE OF CONTENTS

		Page
	Acknowledgments	ii
	Table of Contents	iii
	List of Tables	v
	List of Figures	vi
I.	Introduction	1
II.	Experimental Device	3
	A. High Momentum Spectrometer	3
	B. Low Momentum Spectrometer	4
	C. Vertex Spectrometer	4
	D. Beam and Target	5
	E. Electronics and Triggers	6
	F. On-Line Monitoring	7
III.	Data Reduction Process	9
	A. Data Sample	9
	B. Reduction Chain	9
	C. Data Cuts	12
	D. Biases and Corrections	14
IV.	Results and Interpretation	18
	A. Presentation of the Data	18
	B. Search for Clustering of the Final State Particles	20
	C. Comparison with (p,-) Data	27
	D. Conclusions	30

TABLE OF CONTENTS (cont.)

	Page
Appendix A	32
References	39
Tables	43
Figures	51
Vita	79
Abstract	

LIST OF TABLES

		Page
I.	Spectrometer Characteristics	43
II.	Data Reduction and Cuts	44
III.	Final State Charge Matrix	45
IV.	Detection Efficiencies and Corrected Number of Events For Various n-prong Topologies	46
V.	Percentage of Events For Each Final State Category of Four Prongs	47
VI.	Percentage of Events For Each Final State Category of Six Prongs	48
VII.	Percentage of Events For Each Final State Category of Eight Prongs	49
VIII.	Number of Events For the Dispersion Parameter δ vs. Final State Topology	50

LIST OF FIGURES

		Page
1.	Schematic of the Multiparticle Argo Spectrometer System.	51
2.	Phase Space Acceptances of the HMS and LMS.	52
3.	Schematic of the Vertex Spectrometer.	53
4.	Data Collection and Storage.	54
5.	Computer Program Chain.	55
6.	Average Charge Multiplicity vs. Recoil Mass for Position (1,4).	56
7.	Average Charge Multiplicity vs. Recoil Mass for Position (1,9).	57
8.	Average Charge Multiplicity vs. Recoil Mass for Position (2,4).	58
9.	Average Charge Multiplicity vs. Double Recoil Mass.	59
10.	Number of Events for Each Final State vs. the Double Recoil Mass.	60
11.	Average Charge Multiplicity vs. Inelasticity.	61
12.	Number of Pions Backward vs. Number of Pions Forward for Position (1,4).	62
13.	Number of Pions Backward vs. Number of Pions Forward for Position (1,9).	63
14.	Number of Pions Backward vs. Number of Pions Forward for Position (2,4).	64

LIST OF FIGURES (cont.)

		Page
15.	Number of Pions Backward vs. Number of Pions Forward For All Data.	65
16.	Average Charge Multiplicity vs. Recoil Mass For $\langle t \rangle = 0.23$ (GeV/c)^2 in Position (1,4).	66
17.	Average Charge Multiplicity vs. Recoil Mass For $\langle t \rangle = 0.94$ (GeV/c)^2 in Position (1,4).	67
18.	Average Charge Multiplicity vs. Recoil Mass For $\langle t \rangle = 0.25$ (GeV/c)^2 in Position (1,9).	68
19.	Average Charge Multiplicity vs. Recoil Mass For $\langle t \rangle = 1.40$ (GeV/c)^2 in Position (2,4).	69
20.	Average Charge Multiplicity vs. Momentum Transfer For $\langle W' \rangle = 6.13$ GeV/c^2 in Position (1,4).	70
21.	Average Charge Multiplicity vs. Momentum Transfer For $\langle W' \rangle = 4.34$ GeV/c^2 in Position (1,9).	71
22.	Average Charge Multiplicity vs. Momentum Transfer For $\langle W' \rangle = 6.12$ GeV/c^2 in Position (2,4).	72
23.	Average Charge Multiplicity vs. Recoil Mass For $\langle t \rangle = 0.24$ (GeV/c)^2 in Positions (1,4) and (1,9).	73
24.	Average Charge Multiplicity vs. Recoil Mass For $\langle t \rangle = 0.97$ (GeV/c)^2 for Positions (1,4) and (2,4).	74
25.	Average Charge Multiplicity vs. Recoil Mass For Positions (1,4), (1,9) and (2,4).	75

LIST OF FIGURES (cont.)

		Page
26.	Schematic Drawing of a Cylindrical Spark Chamber and Readout.	76
27.	Spark Chamber Assembly With Top Lid Removed.	77
28.	Spark Chamber Efficiency vs. Multiplicity.	78

Chapter I

INTRODUCTION

At the time this experiment was conceived, high energy counter-spark chamber experiments had measured the behavior of one, or at most two, of the final state particles resulting from a high energy interaction.[1] This state of affairs was attributable to two causes. First, instrumentation and techniques were not sufficiently developed to be able to measure multiparticle final states. Bubble chambers, of course, had long been able to detect and analyze multiparticle charged final states, but these experiments were limited by being unable to select a specific type of event or range of variables for study. The second difficulty was a direct consequence of the first. For the instrumental reasons mentioned, only the bubble chambers took multiparticle data, and they collected data with sufficient statistics only on the most abundant processes at low incident energies whose final states were characterized by low multiplicity and low momentum transfer to the incident particles. For events of this type, resonance states existed in profusion and were explained in part by peripheral production mechanisms.[2] The remaining effects were thought to be those associated with a phase space background. That this was not the case is attested to by the contents of this thesis.

We recognized early that we knew little about multiparticle final states, let alone the new physics they might contain. So we conceived, designed, built and performed an experiment using a 28.5 GeV/c proton

beam from the Brookhaven National Laboratory Alternating Gradient Synchrocyclotron, producing multiparticle final states after encountering a proton in a hydrogen target. To detect the many charged particles which result from these collisions we created a new and unique multiparticle spectrometer which is a concatenation of the triggerability, data rate and resolution of spark chambers and of the solid angle advantages of the bubble chamber.

The experiment was designed to exploit a picture we had of the anticipated behavior in high energy pp scattering processes. We felt that the protons involved in the reaction were the cources from which pions would be produced in a new, non-peripheral way, provided the collision was sufficiently central. Thus, two conventional single arm spectrometers measured the protons, while a third vertex spectrometer detected most of the associated charged pions. Using this system, we were able to select for analysis only those rare events which were of interest (i.e. central collisions) and ignore the more copiously occurring processes.

We present here some first results from this spectrometer system. We study average multiplicity for final state proton detected events as a function of a variety of variables describing one or both final state protons. We isolate the production process for multipion events by searching for clustering effects of the final state particles. Finally, we compare the average charge multiplicity found here with that from events with only one identified proton.

Chapter II

EXPERIMENTAL DEVICE

This experiment was performed at the Alternating Gradient Synchrocyclotron (AGS) of the Brookhaven National Laboratory (BNL) and used the Multiparticle Argo Spectrometer System (MASS) developed in a BNL-VPI collaboration.[3] The MASS is shown in Fig.1 and consisted of three systems: High Momentum Spectrometer (HMS), Low Momentum Spectrometer (LMS), and Vertex Spectrometer (VS). The HMS and LMS are conventional single particle, wire spark chamber spectrometers. The VS is a new and unique multiparticle detection device. During the experiment nine different triggers were accepted, which required variously a proton and/or pion in the HMS and/or LMS. The VS then detected the charged secondaries resulting from each event which produced a trigger. Here we discuss some of the data where protons were detected in the HMS and LMS. Studies of other reactions appear elsewhere.[4-8]

A. High Momentum Spectrometer

The HMS is essentially the same spectrometer used in two previous experiments at the Alternating Gradient Synchrocyclotron.[9] It was designed to detect a fast (4 - 30 GeV) particle with good angular and momentum resolution and pion/proton particle discrimination. Each of its two dipole magnets bends a 28 GeV/c particle through 2.5^{o}. These magnets are preceded by 4x-y core readout spark chambers and followed by 4x core readout chambers so that momentum analysis is effected. A high pressure (70 psi) gas Cherenkov counter provides for mass identification. This

spectrometer could be positioned in $\sim$ 2 h, and allows data to be collected at a variety of laboratory angles.

Table I summarizes the resolution, solid angle acceptance and operating characteristics for the HMS, LMS, and VS. Fig.2 shows the phase space regions accessible to the HMS and LMS, together with their acceptances at various positions.

B. Low Momentum Spectrometer

The LMS was designed to detect and analyze one of the slower particles ($\frac{1}{2}$ to 4 GeV/c) resulting from an interaction. During data taking most of the particles traversing the LMS had momenta which were in fact below 2 GeV/c. The spectrometer consisted of a large aperture dipole magnet on which was mounted two sets of four magnetostrictive readout chambers each, which bracketed the magnet. One chamber in each set was rotated an angle of 26.5^{o} to the vertical so that tracking ambiguities, which occurred when two particles of an event traversed the spectrometer, could be resolved. A high pressure gas Cherenkov counter provided pion/proton particle identification for particles with momentum 1.5 to 6 GeV/c. Scintillation counters provided time-of-flight (TOF) information which allowed mass identification for particles with momentum below 2.5 GeV/c. This spectrometer could be positioned in 2/3 h and could scan laboratory angles between 0^{o} and 90^{o}.

C. Vertex Spectrometer

The VS was designed to measure most of the charged secondary part-

icles resulting from an interaction as it subtended a solid angle of 2π sr. It consisted of a nested set of nine cylindrical wire spark chambers surrounding a liquid hydrogen target (see Fig. 3). This entire assembly was immersed in the 10 kG magnetic field of the ARGO magnet.[10] The field volume measured 1.5 x 1 x 1 m^3. The chambers had radii varying from 15.25 cm (6") to 47 cm (18.5") with an active height of 73.5 cm. Thus, particles with angles up to $\pm$ 60° from the equatorial plane were detected. The spark gap of each chamber was .95 cm, and high multiparticle efficiency was obtained by pulsing the chambers in a transmission line mode. Spark location was obtained by means of magnetostrictive lines located inside the magnet but shielded from its magnetic field. A detailed description of the chamber construction and performance appears as Appendix A.

D. Beam and Target

For this experiment the MASS was set up in the diffracted proton beam (A2 beam) at the AGS. During each AGS acceleration period a fraction of the circulating protons was extracted by reducing the magnetic field in the main ring by 0.4%. Once external, this slow extracted beam (SEB) was focused onto a 12 cm long beryllium target and the diffractively scattered protons were collimated and entered the A2 beam line at a distance of approximately 156 m from the experiment. The beam was transported, analyzed, and focused by a series of dipole and quadrupole magnets. During the extraction process the energy of the SEB changed, so the currents of the dipole magnets in the A2 beam transport system had to be adjusted in concert with the main ring magnets so

that a uniform intensity beam was available over the entire spill. A measure of the beam momentum was provided by monitoring and recording the magnetic field of the main ring magnets during the spill. At the hydrogen target the beam had a spot size of 0.3 x 1.8 cm^2, an angular divergence of $\pm$ 5 mr in the horizontal plane and < 1 mr in the vertical plane, and a maximum instantaneous intensity of 6 x 10^5 protons/s (see Appendix A). Events caused by the halo of slow particles which accompanied the main beam were eliminated by a veto counter upstream of the target. Events in which two protons could have interacted in the target within the resolving time of the spark chambers were tagged (confusion eliminator flag) and eliminated in the data reduction. The horizontal angle of each interacting proton was determined to 1/2 mr by a 16 element scintillation counter hodoscope placed $\sim$ 10 m upstream of the target.

The liquid hydrogen target was a cylinder 20 cm long and 5 cm in diameter. The vacuum jacket, appendix and reservoir were mounted on rails which were attached to the upstream end of the ARGO magnet, allowing the target to be positioned at the center of the cylindrical chambers without dismantling the VS.

E. Electronics and Triggers

The two external spectrometers provided for nine (HMS, LMS) triggers: pp, pπ, πp, $\pi\pi$, -p, -π, p-, π-, and --. Since there was a wide range of rates for these triggers, we electronically selected the predetermined fraction of events of each trigger type to be accepted during the spill. Typically, we would accept all of the rare triggers (e.g. double arm

triggers) and only enough of the more copious ones to maintain the system at maximum capacity. We usually took 8-10 events per AGS spill because of the limited storage (4 K decimal words) in the memory of our data handler. When a trigger condition was satisfied, all of the spark chambers were fired and the entire system was held "busy" for a preset deadtime, $\sim$ 10 ms. During this deadtime, the spark chambers were interrogated and the digitized spark information was stored in the data handler. The core chambers were read out directly by the data handler, while all of the magnetostrictive chambers were read out by a MIDAS system.[11] In addition ancillary information about the event was also recorded during this time: TOF, trigger type, event number, hodoscope flags, etc. Events were thus recorded until the memory of the data handler was full, at which time its contents were simultaneously recorded on magnetic tape and sent to the on-line computer. A schematic diagram of the data collection and storage process appears as Fig. 4.

F. On-Line Monitoring

During data taking, there were a wide variety of monitoring codes available which enabled the experimenter to be reassured about the quality of the data and to detect obvious malfunctions in the system. Most of the simpler diagnostics were provided by a DEC PDP-9[12] computer located adjacent to the electronics trailer. It had a 5×10^5 bit words data storage drum, a lineprinter, and a CRT display. This system monitored all magnets, power supplies, and the quality of the raw spark data.

A subsample of the data was also shipped over a high speed data link, BROOKNET, to the CDC 6600 for analysis by program ONLINE.[4] ONLINE, which was executed remotely from the PDP-9, provided more detailed information, such as individual chamber efficiencies, physics histograms, target distributions, etc. These results were shipped back to the run trailer where they were printed out. The typical time in this exchange was ½ hour.

Chapter III

DATA REDUCTION PROCESS

The procedures to reduce and collate the data which produced the sample of events for physics analysis are discussed as well as the geometrical constants, calibrations, and systematic biases which resulted.

A. Data Sample

In a three week run in April, 1972, MASS completed a total of $\sim$ 260 data runs, with the HMS and LMS positioned at a variety of angles. The beam intensity was usually $\sim 6 \times 10^5$ protons/s, and occasionally 2×10^6 protons/s. Only the low beam intensity runs,where the cleanest events in the VS occurred,were analyzed. All double-arm proton triggers which occurred when the system was active were accepted. About 15% of the (p,p) triggers were lost because they occurred when the system was storing a previous event. Half of the total number ($\sim$ 16,000) of (p,p) triggers were recorded in four runs where the HMS and LMS were at their smallest angles, position (1,4).

B. Reduction Chain

Figure 5 is a schematic representation of the data reduction chain. The first code, CDT, read a Raw Data Tape and generated a Condensed Data Tape. Calculations were made, from which cuts on the data were effected and failing events were dropped.

Each event on the Condensed Data Tape was stored in segments. The first contained run number, event number, trigger type, incident beam

momentum, hodoscope information, and confusion eliminator flag. The second segment contained contents of the digital voltmeter memory. The raw data was stored in the third segment, so that in subsequent analyses corrections could be made without reference to the Raw Data Tapes. Segments four and five contained the calculated HMS and LMS information, respectively. For each external spectrometer the track was reconstructed, and its momentum, production angles, and the particle type were stored. Segment six contained the calculated information from the VS. For each spark, the raw digitizing was "cleaned", normalization constants were applied, and a quality tag was assigned.

The code PITRACK used the spark digitizings from the VS and, by associating them into helical trajectories, attempted to reconstruct the event.[6] The output from PITRACK contained the coordinates of the event vertex, the charge, number of sparks, and three-momentum for each charged track in the event. Extra beam tracks, tracks not connected to the vertex (e.g. neutral decays) and tracks which could only be associated in two dimensions, were tagged Non-Associated TrackS by PITRACK. The PITRACK solution of an event was appended to the Condensed Data Tape as the seventh segment. All of the (p,p) events on the Condensed Data Tape were processed by PITRACK, except the ones classified as "confused".

The code VUE provided an interactive graphics CRT display of the data and the results of the PITRACK solution.[5] One could then intervene and modify the PITRACK solution of an event by adding or deleting sparks on a track, associating new tracks or eliminating tracks

established by PITRACK. A scanner could process ∿ 15 events/h in this manner. VUE recorded all of the changes made, and the results, containing the scanner's initials, the original and final number of tracks and extras, and a grade reflecting the quality of each event, were stored as the eighth segment on the Condensed Data Tape. VUE also overwrote the seventh segment of the Condensed Data Tape for an event if an amendment to the set of tracks was found necessary by the scanner.

Scanned events were graded according to the following nine classifications:

S: Super - a perfect event, with all tracks clearly identifiable, originating from a common vertex while the unused sparks were distributed randomly.

A: No questionable tracks, no NATS but some unused sparks which might indicate the passage of a particle.

B: No questionable tracks, but NATS present and tagged as such.

C: No questionable tracks, but some unused sparks present which might indicate the passage of NATS.

D: One questionable track from the vertex and either no NATS or identified NATS present.

E: Same criteria as grade C except also contains one questionable track.

F: More than one questionable track.

G: Outside the target volume or double vertex events.

H: Chaos.

A questionable track was one which did not contain sparks in 2/3 of the chambers it should have intersected. Two spark tracks, whose dip angles allowed them to exit the VS after the first two chambers, were also classified as questionable.

The code FIT used an iterative least squares procedure to fit all tracks from the primary vertex to a common intersection point.[13] The fitted vertex coordinates, and momenta and two angles for each track, and a fully correlated error matrix were produced for each event. Events which failed to converge were flagged and were either rescanned or dropped from further analysis. Successfully FIT events were then passed on, subject only to a final target and grade cut.

C. Data Cuts

Table II enumerates the cuts and their effect on the data. The failure to get all the anticipated data from the Raw Data Tape resulted from human error, scaler malfunctions and parity errors.

In the CDT code, cuts were made in hierarchical order, so an event which failed at any step was dropped from further analysis. First the bit pattern of the hardware trigger flag was checked. Since there were eight bits, one for each trigger type, events which had no bits or two or more bits set were illegal triggers. The bit pattern of the 16 element beam hodoscope flag was checked next to see if one or two adjacent bits were set. A reconstruction of the trajectory of the HMS trigger particle was then attempted. Failures occurred because chambers were inefficient, more than one particle traversed the spectrometer or

a particle scattered before reaching the Cherenkov counter. If the HMS particle's trajectory was successfully reconstructed, it was extrapolated through the ARGO magnetic field and was required to intersect the target within liberal margins. After the HMS trajectory had been accepted, the CDT code attempted the same procedure for the LMS particle and performed the same cuts.

In determination of particle type the hardware input and the calculated quantities in the external spectrometer were compared. In the two gave contradictory particle identification, the CDT code resolved the issue. For example, if the HMS Cherenkov counter fired, indicating the passage of a pion, but the particle's momentum was calculated to be greater than 27 GeV/c (for position 1), the particle was defined to be a proton and the appropriate trigger flag was set. For the LMS, which had a less efficient Cherenkov counter, the opposite was usually true; i.e., if the Cherenkov failed to fire, indicating a proton, but the TOF measurement indicated a pion, the particle was defined to be a pion.

All events surviving the cuts in CDT were input to PITRACK, except those classified as confused.

Between the PITRACK step and the FIT output some events were lost at random because of irreversible software errors. A cut was made on grade after FIT and events of quality D and above were accepted. A target cut of $\pm$ 9.65 cm in the longitudinal direction completed the data selection. The final data sample of $\sim$ 1,500 events represents 9.5% of the raw (p,p) triggers.

D. Biases and Corrections

The VS covered less than 4π sr, so some charged particles would escape detection. Therefore, we had to correct for these missed tracks. In first approximation, we did this by adding sufficient tracks to each event to obtain a net final state charge of +2. A corrected charge multiplicity then resulted, whose average value, $\langle n \rangle$, for the sample of 1,500 events was 5.25 ± 0.06. The error is statistical and does not include the systematic effects inherent in the experimental device and analysis.

To check the accuracy of this procedure, we constructed a final state charge matrix, seen in Table III, where the tracks of the trigger protons are not included. Events in the [1,1] element ($1\pi^+$, $1\pi^-$) were topologically four prong events. We now discuss three categories of events which could bias our results: those with missed particles, those with excess particles and those with tracks whose charge is incorrectly assigned.

By scanning the events, we found that $\sim$ 10% of the tracks were not detected by the VS, while $\sim$ 1% were charge ambiguous, high momentum pions and < 1% of the events had excess tracks.

First, we had to correct for tracks which occurred outside the VS detection volume. Here we treated each track of an event as being independent, so for an n prong event the probability for finding one of the n-2 VS tracks was ε_n. The misses were then binomially distributed. For example, for six prong events N_6 was the true number of events, N_6^o the number found (the [2,2] element) and N_6^- the number with

one missing negative particle (the [2,1] element). We wrote two equations with two unknowns, N_6 and ε_6;

$$N_6^o = N_6 \varepsilon_6^4$$

and

$$N_6^+ + N_6^- = \frac{4!}{1!\ 3!} N_6(1 - \varepsilon_6)\varepsilon_6^3 .$$

From Table III, $N_6^o = 269$ and $N_6^+ + N_6^- = 176$, so $\varepsilon_6 = 0.86 \pm 0.02$ and $N_6 = 494 \pm 22$. The ε_n and N_n for the other final states similarly obtained are tabulated in Table IV.

Next we calculated the total number of events expected to have two missing particles,

$$N_n^2 = N_n^{++} + N_n^{+-} + N_n^{--} .$$

For six prongs:

$$N_6^2 = \frac{4!}{2!\ 2!} N_6(1 - \varepsilon_6)^2\varepsilon_6^2 = 43 ,$$

1/6 of which would appear in the [0,2] and the [2,0] elements and 2/3 in the [1,1] element. The double miss contributions, appearing in parentheses in Table III, were added to the appropriate diagonal element.

The non-zero, doubly off-diagonal elements were populated by events where a high momentum pion had an incorrect charge assignment. Scanning revealed that $\sim$ 2% of the events had a negative and $\sim$ ½% had a positive track misassigned. These events had the correct number of tracks and were moved to the appropriate diagonal element. Finally, the remaining off-diagonal elements were corrected by requiring a final state charge of +2. The resulting average charge multiplicity was

$\langle n \rangle = 5.32 \pm .06$, which is consistent with the previous estimate.

From the charge matrix the number of particles not seen by the VS was estimated to be $\sim$ 14%, which was consistent with the detection probabilities calculated above. We investigated the source of these missed tracks by generating Monte Carlo events using the code NVERTEX[14] in the geometry of the VS. The HMS proton was constrained to lie within the acceptance of the external spectrometer and was generated with an exponential momentum transfer dependence. The LMS proton was left free. The events were weighted by

$$Ce^{-b\Sigma|P_T|},$$

where the sum was over the transverse momentum of all the produced secondaries, and C and b were constants related to the number of prongs in each event. Of the particles thus generated $\sim$ 11% would not have been detected, which is consistent with our other estimates.

In addition we tried to determine the losses from the data itself by plotting, for the produced pions, the production angle,

$$\theta = \mathrm{Cos}^{-1}\left(\frac{P_{\parallel}}{|\vec{P}|}\right),$$

versus the azimuthal angle,

$$\phi = \mathrm{Tan}^{-1}\left(\frac{P_y}{P_x}\right).$$

Assuming an isotropic distribution in ϕ, up-down losses can be estimated for $0 \leq \theta \leq 90^{\circ}$. However, for $\theta > 90^{\circ}$, backward losses were also present. By extrapolating the cross-section in θ to 180°, we obtained

losses which were consistent with 14%.

Other effects (< 1%) which caused misses are enumerated but were not considered: slow pions not reaching the second chamber, particles which scattered in the VS, incorrectly tagged NATS and fast pions, part of whose trajectories were in the chamber dead spots.

Chapter IV

RESULTS AND INTERPRETATION

The original data sample of $\sim$ 16,000 events was reduced to $\sim$ 1,500 events, all of which were scanned and fit to a common vertex. Both final state protons were identified experimentally, and we assume that the remaining charged particles are pions.

Here, we give the dependence of the multiplicity on several variables which characterize the (p,p) events. Next, we investigate clustering effects of the final state particles in order to specify the production process. A comparison of our results with those from (p,-) events is then given. Finally, we summarize our conclusions and discuss the future analysis of this experiment which bears on these results.

A. Presentation of the Data

We now study the behavior of the average multiplicity for (p,p) events. The lack of a specific model which could be used as a guide forces us to express these results in terms of the variables on which the data depend most strongly: W and W', the recoiling mass from the HMS and LMS protons, respectively. We then attempt to understand these data in phenomenological terms.

We plot in Figs. 6-8 the average corrected charge multiplicity vs. W, for two intervals of W', for the data from positions (1,4), (1,9), and (2,4) respectively. The data points have been displaced in W for clarity. In all cases, $\langle n \rangle$ rises sharply and linearly with W. No

dependence on W' is seen, which may be because the range of this variable is limited in each position. However, the <n> from position (1,4), which has larger average W', is consistently higher than for position (1,9), the disparity increasing with W.

This strong dependence of <n> on the recoil mass from either proton can be understood in terms of a fragmentation model of particle production.[15] In this picture, a small value of W indicates that the secondary particles were produced by the single fragmentation of the recoil proton into a small mass, low multiplicity final state. Similarly, a large W would indicate the fragmentation of both protons, yielding a higher multiplicity final state. Since pp scattering is symmetrical we expect the same reasoning to hold for W'. We postpone further discussion of this behavior until Section B, where a more detailed analysis is presented and which strengthens our belief in the correctness of the fragmentation model.

The average charge multiplicity for all the data, as a function of the recoil mass from both protons, the double mass W'', is seen in Fig. 9. Again we see a linear increase of <n>. Further, as we see in Fig. 10, increasing W'' kinematically allows for higher charge multiplicity final states so few prong events dominate at low W'' and many prong at large W''. This effect is partially responsible for the linear increase in the average multiplicity.

The average charge multiplicity vs. the inelasticity, K, defined as

$$K = \frac{s^{\frac{1}{2}} - E^* - E'^*}{s^{\frac{1}{2}} - 2m} ,$$

where $s^{\frac{1}{2}}$ is the total center-of-mass energy, m the proton mass, and E* and E'* are the energies of the HMS and LMS protons in the center-of-mass, respectively, is plotted for the whole data sample in Fig. 11. Inelasticity, a fractional measure of the energy available for particle production, varies between 0, elastic and 1, both protons at rest in the center-of-mass. The linear increase of <n> with K indicates that many low energy secondaries are produced as the energy available from the protons increases.[16] A process in which the energy is transferred to a small number of secondaries would show a much weaker dependence of <n> on K.

We checked the dependence of <n> on other variables which describe the behavior of the two protons, such as the four-momentum transfer t and the transverse momentum, P_T. We find no strong dependence on these variables discernible with our statistics.

B. Search for Clustering of the Final State Particles

We now find the production mechanism responsible for our multiparticle final states. Current theories are all able to fit some portion of the pp scattering data but they describe the production of pions in distinctly different ways. For example, diffractive fragmentation models[15] view the pions as boiling off from the two protons, while in multiperipheral models[17] the pions are produced as a result of a multiple exchange process between the two protons. Since we have detected both final state protons in our data sample, we are able to look for clustering effects among the final state charged particles.

The clustering is very different in these two models. Difficulties arise however when one attempts to establish unambiguous criteria for associating certain pions into clusters, difficulties which are exascerbated as the incident energy is lowered.

We assume that pions which go into the backward center-of-mass hemisphere are associated with the LMS proton and forward going pions with the HMS proton. We plot the average number of backward versus forward pions, and vice versa,in Figs. 12-15 for three different spectrometer positions and the entire data sample. These multiplicities are derived from detected pions only and have no correction for missed tracks.

We note first that the backward/forward pion ratio is $\sim$ 2:1 for all the positions implying that for our data, the pions are more often associated with the recoil target proton than the fast beam proton. This is a consequence of the detection constraints on the protons and we expect that data which doesn't constrain the protons would show an equal number of pions in each hemisphere. Second, the average number of produced particles changes with the position of the external spectrometers. In position (1,4) $\sim$ 3 pions are produced on the average, while only $\sim$ 2 pions are produced in position (1,9). This effect will be investigated in more detail in the following section where we compare our data with a sample of (p,-) data. Finally, the average number of pions produced in each hemisphere is remarkably constant. This is a strong indication that the two protons are fragmenting and doing so independently. A recent result from the Intersecting Storage Ring at

CERN[18] at considerably higher center-of-mass energy, 31 GeV vs. our 7.5 GeV,shows this effect in data where the average multiplicity is much larger ($\sim$ 10).

A more quantitative investigation of clustering of the final state charged particles is now called for. Since the secondaries produced in pp scattering have an exponentially damped transverse momentum distribution centered at $\langle P_T \rangle \sim 300$ MeV/c,[16] we expect that clustering effects will be most prominent in the longitudinal direction. We therefore need a variable which enhances the longitudinal behavior of the particles. Such a variable is the rapidity,[19] defined in the laboratory frame as,

$$y = \frac{1}{2} \ln\left[\frac{E + P_{\parallel}}{E - P_{\parallel}} \right] = \tanh^{-1}\left(\frac{P_{\parallel}}{E}\right),$$

where E is the energy of the particle and $P_{\parallel}$ the longitudinal component of the momentum. Rapidity is not Lorentz invariant, but the difference between any two rapidities is.

Rapidity is a good variable for us to use since pions which are associated with one of the protons should have a rapidity similar to that of the proton to indicate a fragmentation process. Pions which are produced in a multiperipheral process should be randomly distributed in rapidity.

In this analysis we first select events that have charge balance in the final state,thus eliminating biases arising from non-detected particles. We then categorize every four prong event as belonging to one of four production processes, the first three of which are

fragmentation type events, while the fourth is a multiperipheral type: 1. (p) ($\pi\pi$p'), 2. (pπ) (πp'), 3. (p$\pi\pi$) (p'), 4. (p) ($\pi\pi$) (p'), where p is the HMS and p' is the LMS proton and the parentheses denote clusters.

For six prong events, the possible processes are: 1. (p) ($\pi\pi\pi\pi$p') 2. (pπ) ($\pi\pi\pi$p'), 3. (p$\pi\pi$) ($\pi\pi$p'), 4. (p$\pi\pi\pi$) (πp'), 5. (p$\pi\pi\pi\pi$) (p'), and for eight prongs: 1. (p) ($\pi\pi\pi\pi\pi\pi\pi$p'), 2. (pπ) ($\pi\pi\pi\pi\pi\pi$p'), 3. (p$\pi\pi$) ($\pi\pi\pi\pi$p'), 4. (p$\pi\pi\pi$) ($\pi\pi\pi$p'), 5. (p$\pi\pi\pi\pi$) ($\pi\pi$p'), 6. (p$\pi\pi\pi\pi\pi$) (πp'), 7. (p$\pi\pi\pi\pi\pi\pi$) (p'). No attempt is made to look for multiperipheral type events here because the separation in rapidity values at our energy is not great enough to make an unambiguous determination.

The following criteria are used to decide on the category for each event: if $|y_{p'} - y_{\pi}| < |y_p - y_{\pi}|$ the pion was associated with the slow LMS proton and vice versa. In addition, four prong events of type four were characterized by

$$|y_{\pi 1} - y_{\pi 2}| < |y_p - y_{\pi i}| \text{ and } |y_{\pi 1} - y_{\pi 2}| < |y_{p'} - y_{\pi i}|,$$

where i = 1,2.

The validity of the results from this procedure can of course be impuned because π^o are produced which are undetectable by MASS. Thus, events which appear to result from an unambiguous single fragmentation process may indeed be double fragmentation with one or more π^o's associated with the protons. It is not possible to determine the frequency of these neutral pion processes from our data but we have made two attempts below to estimate their magnitude. Tables V-VII

contain the percentage of events for each process for four, six and eight prong events in positions (1,4), (1,9) and (2,4). An analysis was not done for position (1,9) eight prongs since there were only five events. At all positions for four prongs,the largest fraction of the events are type 1, fragmentation of the LMS proton, while only $\sim$ 10% of the events are of the multiperipheral type. An estimate of the contamination due to double neutral pion production can also be made from Table V by noting that type 3 processes occur $\sim$ 1% of the time. Assuming that the fast proton produces two π^o with the same frequency as $\pi^+\pi^-$ we believe that double π^o production also occurs $\sim$ 1% of the time. Single π^o production, however, may still be a large effect.

As the multiplicity of the final state increases the dominance of type 1 processes lessens and other processes occur more frequently. The conclusion we draw is that low multiplicity final states for our trigger configuration are produced by single fragmentation, while as the multiplicity increases so do the occasions of both protons fragmenting. Also a dependence on the position of the external spectrometers can be observed since the six prong events in positions (1,4) and (2,4) are more strongly peaked toward single fragmentation than in position (1,9). As is seen in Fig. 2, position (1,4) and (2,4) constrain the two protons to vastly different regions of phase space, while position (1,9) is a more symmetrical case.

To check that the rapidity criteria is valid, we have calculated the effective mass, M, of all combinations of particles in four prong

events by

$$M = [(\sum_{i=1}^{m} E_i)^2 - (\sum_{i=1}^{m} \vec{P}_i)^2]^{\frac{1}{2}}.$$

If the association of particles based on the rapidity criteria is correct, we expect that the effective mass of these combinations will be low (typically $M < 1.7$ GeV/c^2), while incorrect associations will have a mass above that. We find that $\sim$ 95% of the cluster associations based on rapidity had their effective mass in the appropriate range, giving us confidence that the rapidity selection criteria are valid.

We can make another check on this procedure and get another estimate of π^o production by calculating W, the recoil mass from the HMS proton, for each event. We assume that events with $W < 3.0$ GeV/c^2 seldom have pions associated with the HMS proton, while events with a W above this value are ones where we would expect double fragmentation. We found that $\sim$ 48% of all four prongs in position (1,4) had $W < 3.0$ GeV/c^2, as opposed to 12% of the six prongs and none of the eight prongs. This behavior supports the result of the previous section concerning the rise of the multiplicity with W. Second, since all of the eight prongs have $W > 3.0$ GeV/c^2, the events classified above as type 1 for this final state are probably double fragmentation with at least one π^o associated with the HMS proton. Thus, our conclusion above that high multiplicity final states procede via double fragmentation is strengthened.

Finally, following a suggestion by Berger, Krzywicki and Fox,[20] we took a statistical approach and calculated a dispersion parameter

which is a measure of the spread of the rapidities in each event. The average rapidity for any n prong event is defined as

$$\bar{y} = \frac{1}{n} \sum_{i=1}^{n} y_i .$$

Then, to eliminate the leading particle, which would tend to spuriously broaden the distribution, we discard the rapidity y_k satisfying

$$|y_k - \bar{y}| = \{\max|y_i - \bar{y}|, \; i = 1,n\}.$$

After rejecting this y_k we define the dispersion, δ, as

$$\delta = \left(\frac{1}{n-2} \sum_{i=1}^{n-1} (\bar{y} - y_i)^2 \right)^{\frac{1}{2}}.$$

Berger et.al. predict that events representing single fragmentation should be centered around the value $\delta \simeq 0.9$, while double fragmentation events should have a somewhat larger δ. In both cases δ will be independent of the final state multiplicities. Multiperipheral type processes should have a δ which increases with the final state multiplicity.

The data from position (1,4) were used to generate Table VIII, which shows that δ does not depend on the final state multiplicity, thus indicating that fragmentation type processes dominate. Unfortunately our incident energy is not great enough to give the larger dispersion values so this result is not definitive. For position (1,4), the range of rapidities observed is from 4 to -1. If eight particles are produced in this range, there is a limit to the value of δ which may obscure the results.

C. Comparison with (p,-) Data

Using data in which the HMS proton triggered MASS, (p,-), the behavior of the average charge multiplicity was found as a function of two independent variables to be

$$N(t,W) = 2 + A_1(W - m) + (A_2 t - A_3)(W - m)^2,$$

where m is the proton mass and t is the momentum transfer to, and W, the recoiling mass against the trigger proton.[6] The constants were $A_1 = 1.19 \pm .033$, $A_2 = 0.011 \pm .001$ and $A_3 = 0.114 \pm .01$.

Since both protons provided the trigger for our data sample, (p,p), and thereby kinematically constrained the events, we compare and contrast our data with the (p,-) parameterization. The (p,-) events were not scanned, as there were $\sim$ 14,000 of them, and there was a known bias which resulted from relying on the PITRACK code alone to give the multiplicity. Therefore, an overall correction of 0.15 tracks/event was added to the (p,-) results before they were compared with our data, which have all of been scanned.

In Figs. 16 and 17, we plot the average charge multiplicity, <n>, for events in position (1,4), for two t intervals, as a function of W. The solid curve is the (p,-) result, calculated using the average t of each interval. In both cases, the <n> from the (p,p) triggers are higher than those from (p,-), the disparity increasing with W and independent of t. The uncertainties shown on the (p,p) data are statistical only, and merely reflect the number of events in each bin. No attempt has been made here to evaluate and include systematic errors.

A typical error for the (p,-) function, derived from the uncertainties in the fitted coefficients, was found to be $\sim$ .02 particles and is not shown in the figures.

In Fig. 18 we plot similar distributions from the position (1,9) data. We see here that the results from both triggers agree within errors.

To understand this behavior, we refer to Fig. 2. The majority of the (p,-) events came from the high cross-section region of phase space, in which the recoil proton goes strongly backward. This region is characterized by small W and low multiplicity final states indicative of distinguishable isobar production. For (p,p) triggers, the region spanned by position (1,4) is far from the isobar region and could be characterized as having more central collisions, with expected higher multiplicity final states. Events from position (1,9) are closer to the isobar region and therefore should agree with the results from the (p,-) data.

To check this deduction, we plot the data from position (2,4) events in Fig. 19. Here, the recoil proton is again constrained to lie in the central region of phase space and the multiplicity is higher than for the (p,-) trigger.

Further evidence can be found by reversing the roles of the two protons: in position (1,4) the HMS proton will lie in the isobar region if it is viewed as the recoil proton. The two relevant variables are then t', the momentum transfer to, and W', the recoiling mass from, the LMS proton. We now expect the (p,p) multiplicity to be lower than

the (p,-) since the recoil HMS proton is now constrained entirely to the isobar region and there are no small cross-section, high multiplicity events present. The results, shown in Fig. 20, fulfill our expectations.

For the position (1,9) data, shown in Fig. 21, the difference between the (p,p) data and the (p,-) is approximately the same as for position (1,4), as is expected since the HMS proton has been constrained to the same phase space region. For the position (2,4) data, we expect the (p,p) multiplicity to increase somewhat, relative to the (p,-), since now the HMS proton has been constrained to lie somewhat further away from the isobar region. This is indeed the case, as seen in Fig. 22.

To emphasize the change in the multiplicity with position, we plot $\langle n \rangle$ vs. W for positions (1,4) and (1,9) for the interval $0.0 < t < 0.4$ $(GeV/c)^2$ in Fig. 23. As expected, the average multiplicity from position (1,4) is systematically higher than that for position (1,9). In Fig. 24, the data from positions (1,4) and (2,4) are consistent within statistics, reflecting the rather weak dependence of multiplicity on t for fixed W.

To improve the statistics, the data was summed over t and displayed in Fig. 25 is $\langle n \rangle$ vs. W for all three positions. The increase in $\langle n \rangle$ for position (1,4) over that for position (1,9) is now more apparent, especially at large recoil mass values. We checked and found that the average value of t was equal within statistics for each W bin. A comparison between positions (1,4) and (2,4) is more difficult,

since the average values of t were not the same for each W bin. We therefore use the (p,-) function to correct for the differing t values. For W = 4.5 GeV/c^2, the function predicts that the (2,4) data should be higher than the (1,4) data by $\sim$ 0.1 particle. Similar corrections were made for the other values of W, and the two sets of data points are equal within statistics.

Finally, we sum Fig. 25 over W and obtain an overall multiplicity for each position. This yields $\langle n \rangle = 5.16 \pm 0.08$ for position (1,4), $\langle n \rangle = 4.07 \pm 0.14$ for (1,9) and $\langle n \rangle = 6.07 \pm 0.18$ for (2,4). The average W in each position is 3.44, 2.82, and 4.28 GeV/c^2, respectively. If we take an average t and use these values of W in the (p,-) function, we find that the multiplicity from positions (1,4) and (2,4) should differ by $\sim$ .6 particles, an amount consistent with the observed result. However, the multiplicity from (1,9) and (1,4) should differ by $\sim$ .4 particles, which is in disagreement with the (p,p) data. This extra increase in the multiplicity must be due to some dynamical effects associated with the LMS proton.

D. Conclusions

In our study of the reaction $pp \rightarrow pp\,(n\pi^{\pm})$ we found certain regularities governing the production of these multipion final states.

The average charge multiplicity varied strongly and linearly with the recoil mass from each proton individually, W and W', as well as with the recoil mass from both protons, W''. The increase as a function of W is explained by the fragmentation of the LMS proton, with the

fragmentation of the HMS proton becoming increasingly important at large W. The linear dependence of the multiplicity on W'' is understood by the increasing ordering of prong topologies and their abundances. The multiplicity was also found to vary linearly with the inelasticity, indicating that as more energy becomes available from the two protons, more pions will be produced in the final state.

A rapidity analysis yields evidence of clustering of the final state particles which is explained by the fragmentation of the target proton for low multiplicity final states, with the projectile proton becoming increasingly fragmented as the multiplicity increases. The protons fragment independently of each other for all multiplicities. No evidence for multiperipheral type production processes was found.

By comparing our events with those in which only one proton was detected, we find that the average multiplicity depends strongly on the behavior of both final state protons. Constraining the protons to central regions of phase space causes the average multiplicity to increase by $\sim$ 1 particle over that found for isobar processes. This indicates that a central as distinct from a peripheral process is occurring.

There exists $\sim$ 8 times the number of (p,p) triggers in the current data from MASS than was analyzed here. Its analysis will not only improve the statistics but will extend the range of the variables examined here. This data will include events from intermediate LMS positions which will allow checks on the consistency of our results over the entire LMS acceptance region.

Appendix A

CONSTRUCTION AND PERFORMANCE OF THE VERTEX SPECTROMETER

The VS, designed and built for use in this experiment, is a unique detection device possessing the large solid angle advantage of a bubble chamber and the triggerability, digitized readout, and high data rates of spark chambers. It utilizes unique cylindrical spark chambers with high multiparticle efficiency which were developed for this experiment and were built by the Physics Design Group at Brookhaven National Laboratory.

A. Chamber Construction

The chamber electrodes were constructed from commercially available 50 μ Kapton (H-film)[21] bonded to a 25 μ aluminum backing. This foil was stretched over a wooden cylindrical drum, Kapton side up, and a thin layer of epoxy[22] was applied onto which 130 μ gold plated copper wire was continuously wound with a pitch of 12.5 wires/cm. A strong bond between the wires and the backing foil resulted while the top surface of the wires remained exposed to permit spark formation. The wires and backing foil were electrically connected, half the wires at the top and half at the bottom of the cylinder, by bonding a copper strip to the aluminum with conducting epoxy[23] and soldering the wires to the copper. To prevent edge sparking the free ends of the wires were cut back and buried inside the chamber end structure.

A half chamber was constructed by epoxying a 76 μ mylar sheet, which was stretched over an assembly drum, to a metal chamber skelton consisting

of steel (type 1010) headers at the top and bottom, stainless steel vertical support bars at $\pm$ 90° from the forward direction, and vertical aluminum support bars at the edges of the chamber. Nylon honeycomb[24] (cell size 0.95 cm, height 0.95 cm, wall thickness 25 microns) was epoxied to the mylar in the interior of the metal skeleton. The electrode foil was stretched and epoxied wire side up to the skeleton and the honeycomb. The high voltage electrode was isolated from the steel by 2 mm lucite and the ground electrode by 50 μ of Kapton tape. Steel spacer rings, similarly insulated, were placed at the top and bottom of the active chamber area. These rings together with vertical lucite spacer bars, located at the edges of the active area, maintained the 0.95 cm gap spacing.

Two half chambers were joined and removable steel T-caps were attached to the steel headers to form a cavity for the magnetostrictive lines and their readout coils. With the headers imbedded in a steel plate the magnetic field inside the cavity was reduced ten-fold. A finished chamber withstood large forces, contained little material in the active area (0.25 g.), and maintained the gap spacing to $\pm$ .02 cm.[25] The high-voltage electrode had wires parallel with the axis of the cylinder while the ground electrode had wires at either +26.5° or -26.5° with respect to the axis. Because half of each electrode's wires were soldered at the bottom of the foil and half at the top, we were able to detect sparks over the total area of both electrodes. Figure 26 shows a drawing of a typical chamber.

B. Chamber Readout

Each header cavity contained two magnetostrictive lines (0.3 x 0.13 mm^2 Remendur[26] ribbon) whose velocity was premeasured. Pickup coils, 40 turns of #40 copper wire, were located at both ends of each line inside cylindrical biasing magnets.[27]

The readouts, built as complete units, consisted of two lucite strips formed to the correct radius with grooved notches to house the magnetostrictive lines. Curved copper boxes, which contained pickup coils, biasing magnets, insulated standoffs and clay to damp out signal reflections, were epoxied onto the ends of the lucite. The magnetostrictive line, inserted into a teflon tube (diameter 0.8 mm), was wound with a solenoidal biasing coil which provided the capability of polarizing the magnetostrictive line remotely. The line assembly was then placed into the groove in the lucite strip.

The lucite carriers were fitted to the chambers and shimmed tightly against the wires of the electrodes (the distance between the chamber wires and the magnetostrictive line was approximately 1 mm). The pickup coil and solenoid leads were soldered to cable connectors mounted on another copper box attached to the chamber. Shielded twinex cables carried the signals to the amplifiers,[28] located 3 m from the magnet.

The signals from the chambers were digitized by a MIDAS[11] system located in the electronics trailer $\sim$ 30 m from the amplifiers. The minimum spark separation resolvable was 3 mm. Each pickup coil was assigned either four or six scalers. Since each magnetostrictive line had two coils and each line read half of an electrode, a chamber was capable

of recording up to 24 sparks. If the number of sparks was less than the maximum, the double coil readout provided a consistency check. Because fiducial wires were not mounted on the chambers, the scalers were started by a fast logic signal.

The steel headers of the chambers were designed to minimize the effects of the 10 kG magnetic field on the magnetostrictive lines. We found that the lines were unaffected by magnetic fields of 1.5 kG normal to and $\sim$ 40 G parallel to the wire.[29] Thus the lines were oriented perpendicular to the main field component. The normal component seen by the readout wire in the magnet was $\sim$ 1 kG while the 10% field non-uniformity caused the longitudinal component to be as high as 100 G in some places close to the magnet coils resulting in small dead spots and signal inversion on a few of the lines. Digitizings from an inverted signal had a distinctive double-spark pattern and occurred away from the forward direction, so they were averaged by software without loss of resolution.

C. Chamber Operation

To obtain a high multiparticle efficiency, the chambers were operated in a transmission line mode.[30] The high voltage and ground were connected to the aluminum backing sheet instead of to the wires directly. In addition, each chamber was terminated into a resistor-diode combination which matched the inherent chamber impedance, typically 5Ω. This resulted in a uniform high voltage pulse with a rapid rise time over the entire chamber area, while reducing the voltage reflections from the end

structure. The chambers were operated with standard spark chamber gas (90% Ne - 10% He) bubbled through isopropyl alcohol at 0^{o}C which provided the quenching agent. This mode of operation produced sparks with relatively uniform signal height and reduced spark robbing effects.

The chambers had an operating voltage of 5 kV and were pulsed with an HY-13 hydrogen thyratron,[31] which produced a negative high voltage pulse with a 20 ns risetime and 400 ns RC decay time. A regulated high voltage power supply[32] and recharge circuit[33] was capable of operating at rates of 100 pulses/s; the chambers were normally operated with a 10 ms dead time. A +80 d.c. and a +500 V pulsed (2 ms width) clearing field were used to keep the chamber free of electrons. These conditions resulted in a single particle memory time with chamber efficiency down to 30% of $\sim$ 1.5 μs. Delay time between particle passage and the high voltage pulse was 550 ns.

D. Spectrometer Assembly

The completed spark chamber system, which consisted of six full-round (270^{o} active area) and three half-round chambers (180^{o} active area), is shown in Fig.27 . Each chamber header was placed in a groove in the bottom plate of the support structure. The chambers were then aligned, high voltage and readout cables attached, and the assembly completed by placing a top plate over the chamber headers and bolting it into place. The steel plates and chamber headers formed a continuous plate-like extension of the pole pieces, so we substantially reduced the magnetic field components on the lines without altering the magnetic field homo-

geneity in the gap. The assembly was inserted into the ARGO magnet by removing a plug in the magnet top pole piece. The liquid hydrogen target was then introduced into the upstream median spacer gap of the magnet and positioned at the center of curvature of the six full-round chambers. The particles produced in the target and destined for the external spectrometers passed through a 6" gap about the median plane of the magnet and chamber support structure.

The support structure prevented damage when the magnetic field interacted with the chamber headers. This was accomplished by adding 1 cm of steel to the bottom and top plates which resulted in magnetic forces which stretched rather than compressed the chambers. The degree of stretching was adjusted by set screws inserted through the top plate: a 10 kG field caused a stretching force of $\sim$ 3/4 tons.

E. Spectrometer Performance

Because of high instantaneous beam rates we deadened each chamber where the beam traversed it by epoxying 0.25 mm Kapton to its electrodes. Sparks from beam halo, knock-on's, delta-rays and interactions near the target limited our beam intensity to $\sim 6 \times 10^5$ protons/s.

The high multiparticle efficiency which was a cardinal feature of our chambers is shown in Fig. 28. These efficiencies were calculated by reconstructing a sample of events, calculating the number of sparks expected for each track and comparing it with the number of sparks actually found as a function of the number of prongs detected. Efficiencies determined in this way may be biased as tracks had to be found before the

efficiency was calculated. Thus, we next extrapolated externally measured particle trajectories into the VS and counted the number of sparks found in the predicted location. The average multiplicity of these events was $\sim$ 5 and the efficiency 96.5%. Finally, we took elastic events, predicted the path of the recoil proton from the information of an external spectrometer, and found a 2-prong efficiency of $\sim$ 99.7%. That this efficiency is slightly higher than the others may be accounted for by the large ionization of the slow recoil protons.

The spatial resolution of the chamber was measured with the magnetic field on and off. For field-off runs, a straight line fit was made to the particle trajectories as found from the spark location from the vertical wires. A "fit minus measurement" distribution was then constructed which was found to be $\pm$ 0.5 mm wide at half maximum. For field-on runs, the vertical wire sparks were fit to a circle with corrections applied to account for the electron drift resulting from the crossed electric and magnetic fields (e.g. 3.3 mm at $\sim$ 10 kG).[34] These "fit minus measurement" distributions also had a value at half maximum of $\pm$ 0.5 mm.

REFERENCES

1. For example, E.W. Anderson, E.J. Bleser, G.B. Collins, T. Fujii, J. Menes, F. Turkot, R.A. Carrigan, R.M. Edelstein, N.C. Hien, T.J. McMahon and I. Nadelhaft, Phys. Rev. Letters. 19, 198 (1967).
2. For example, K. Gottfried and J.D. Jackson, Nuovo Cimento 33, 309 (1964).
3. E.W. Anderson, G.B. Collins, F. Turkot, S.P. Almeida, J.R. Ficenec and W.P. Trower, "BNL A.G.S. Proposal #396, Study of Multiparticle Production in pp Interactions at 28 GeV/c", (1968).
4. T.S. Clifford, Ph.D. Thesis, Virginia Polytechnic Institute and State University, 1973, unpublished.
5. D.R. Gilbert, Ph.D. Thesis, Virginia Polytechnic Institute and State University, 1973, unpublished.
6. W.N. Schreiner, Ph.D. Thesis, Virginia Polytechnic Institute and State University, 1973, unpublished.
7. G.P. Larson, Ph.D. Thesis, University of Wisconsin, 1973, unpublished.
8. A. Ramanauskas, E.W. Anderson, G.P. Fisher, N.C. Hien, E. Lazarus, K.M. Moy, P. Schübelin, A.M. Thorndike, F. Turkot, L. von Lindern, T.S. Clifford, G.B. Collins, J.R. Ficenec, D.R. Gilbert, W.N. Schreiner, B.C. Stringfellow, W.P. Trower, A.R. Erwin, G.P. Larson, L.J. Gutay, A. Laasanen, K. Stanfield, R.B. Willmann, E. Harvey and W. Selove, Observation of Increasing Charged Multiplicity as a Function of Transverse Momentum in 28.5 GeV/c pp Interactions, submitted to Phys. Rev. Letters, 1973.

9. AGS #256 and AGS #312. It is described in E. Bleser, G.B. Collins, J. Fischer, R. Fujii, S. Heller, W. Higinbotham, J. Menes, H. Pate and F. Turkot, Nucl. Instr. and Meth. 44, 1 (1966).

10. On loan from the Cambridge Electron Accelerator and described in A. Buffington, D.H. Frisch, S. Smith, and C.E.W. Ward, Nucl. Instr. and Meth. 67, 157 (1969).

11. Science Accessories Corp., Southport, Connecticut 06490.

12. Digital Equipment Corp., Maynard, Massachusetts 01754.

13. D.E. Fries, CIRCE - A General Multi-Prong Fitting Computer Program For Spatial Coordinates in a Non-Uniform Magnetic Field, SLAC Report #99, 1969. Modified for our use by R.B. Willman and D.R. Gilbert.

14. C.A. Bordner, A.E. Brenner and E.E. Ronat, Rev. Sci. Instr. 37, 36 (1966).

15. For example M. Jacob and R. Slansky, Phys. Letters 37B, 408 (1971); M. Jacob and R. Slansky, Phys. Rev. D5, 1847 (1972); E. Berger, Fragmentation Models for Particle Production, ANL/HEP 7220 (1972).

16. For example, F. Turkot, Proc. Topical Conf. on High Energy Collisions of Hadrons, Geneva, CERN 68-7 (1968).

17. For example, W.R. Frazer, L. Ingber, C.H. Mehta, C.H. Poon, D. Silverman, K. Stowe, P.D. Ting and H.J. Yesian, Rev. Mod. Phys. 44, 284 (1972).

18. Pisa-Stony Brook Collaboration, 16th International Conf. on High Energy Physics, Batavia 1, 279 (1972).

19. For example, R.P. Feynman, Phys. Rev. Letters 23, 1415 (1969); J. Benecke, T.T. Chou, C.N. Yang and F. Yen, Phys. Rev. 188, 2159 (1969).

20. E.L. Berger, A. Krzywicki, G. Fox, A New Experimental Method For Discriminating Between High Energy Models For Multiparticle Production, ANL/HEP 7230 (1972).

21. Sun Chemical Company, Facile Div. 185 6th Ave., Paterson, New Jersey 07355.

22. Scotch Cast brand epoxy, Resin #8 - Cure time, 70% in 24 hours, 100% in 7 days. 3-M Company, St. Paul, Minnesota 55101.

23. Bipak Conducting Epoxy, manufactured by Emerson and Cummings Company, Canton, Mass. 02121.

24. American Cyanamid Company, Havre De Grace, Maryland, 21078.

25. Further details concerning the chamber construction may be obtained from J. Fuhrmann, Physics Design Group, Brookhaven National Laboratory.

26. "Remendur" is an alloy of 49% Fe, 49% Co and 2% V manufactured by William B. Driver Company, Newark, New Jersey 07102.

27. V. Perez-Mendez and J. Pfab, Nucl. Inst. and Meth. 33 (1965) 141; S. Miyamoto, Nucl. Inst. and Meth. 35, (1965) 323.

28. Designed by J. Fischer and S. Shibata, Instrumentation Division, Brookhaven National Laboratory.

29. L. Kaufman, V. Perez-Mendez and J. Pfab, Preprint UCRL-16536 (March 1966); M.L. Marshak and S.M. Pruss, Nucl. Inst. and Meth. 62, (1968) 295; I.A. Golutvin, Yu. V. Zanevsky, Yu. T. Kiryushin,

V.D. Pshekhonov, V.D. Ryabtsov and I.M. Sitnik, Nucl. Inst. and Meth. 67, (1969) 257.

30. R. VanTuyl, K. Lee and V. Perez-Mendez, LRL Report UCID 3099 (Sept. 1967); J. Fischer and S. Shibata, IEEE Trans. Nucl. Sci., NS-15, No. 3 (1968) 572; O.C. Allkofer, C. Grupen and G. Maxion, Nucl. Inst. and Meth. 79, (1970) 181.

31. Thyratron manufactured by E.G. and G. Co., 160 Brookline Ave., Boston, Mass., 02215. The pulsers were designed and assembled by J. Fischer and his group, Instrumentation Div., Brookhaven National Laboratory.

32. 10 kV unregulated power supply manufactured by Universal Voltronics Corp., 27 Radio Circle Drive, Mt. Kisco, N.Y., 10549.

33. The power supply regulator and fast recharge circuit designed by J. Fischer, Instrumentation Div., Brookhaven National Laboratory.

34. K.R. Bentley, J.D. Davies, J.D. Dowell, C. McLeod, T.J. McMahon, H.B. Van der Raay, T.G. Rhoades, F.J. Wickens, C.J.S. Damerell, R.J. Homer, and M.J. Hotchkiss, Nucl. Inst. and Methods 104, (1972) 299.

TABLE I. SPECTROMETER CHARACTERISTICS

Spectrometer	HMS	LMS	VS
Solid Angle (mr^2)	33 x 10	180 x 47	2π sr
Momentum Acceptance (GeV/c)	5 - 28.5	.6 - 10	--
Resolution $\Delta\theta$ (mr)	$\pm$ .2 (P = 20 GeV/c)	$\pm$ 1.0 (P = 2 GeV/c)	$\pm$ 4 (forward) $\pm$11 (side)
Resolution $\Delta P/P$ (%)	$\pm$ ¼ (P = 20 GeV/c)	$\pm$ ½ (P = 2 GeV/c)	$\pm$ 2 (forward) $\pm$10 (side) (P = 1 GeV/c)
Mass Identification	Yes	Yes	No
Data Rate (events/s)	100	40	20
Movement Time (hours)	2	1	--

TABLE II. DATA REDUCTION AND CUTS

	Per Cent Surviving	(p,p)Events
Raw Data Sample	100.0	15,787
Input to CDT	99.6	15,724
CDT Cuts:		
Illegal Trigger Types	89.1	14,066
Hodoscope Failures	85.7	13,529
HMS Track Reconstruction	70.0	11,050
HMS Vertex Cut	48.2	7,609
LMS Track Reconstruction	41.6	6,567
LMS Vertex Cut	28.8	4,547
Particle Identification Changes ($p \rightarrow \pi$)	13.2	2,084
Surviving Events	13.2	2,084
Confused Events Cut	12.7	2,005
PITRACK Cut	12.6	1,989
Scanning Cut	12.1	1,910
FIT Cut	11.3	1,784
Final Target and Grade Cut	9.5	1,507

TABLE III. FINAL STATE CHARGE MATRIX

NUMBER OF POSITIVE PIONS							
6				1	2		
5				5 (1)	2	1	
4		3	8 (3)	14	16 (1)		
3	1	18 (6)	40	98 (8)	8		
2	15 (7)	96	269 (16)	40	2 (3)	1	
1	115	413 (29)	80	10 (5)	1		
0	146 (26)	93	9 (7)				
	0	1	2	3	4	5	6

NUMBER OF NEGATIVE PIONS

TABLE IV. DETECTION EFFICIENCIES, ε_n, AND CORRECTED NUMBER OF EVENTS, N_n, FOR VARIOUS n - PRONG TOPOLOGIES

n	4	6	8	10	12
ε_n	.80 ± .03	.86 ± .02	.88 ± .02	.85 ± .04	.83 ± .09
N_n	647 ± 25	494 ± 22	211 ± 16	57 ± 8	6 ± 3

TABLE V. PERCENTAGE OF EVENTS FOR EACH FINAL STATE CATEGORY OF FOUR PRONGS

Position	# Events	Type			
		1	2	3	4
(1,4)	205	69.8 ± 5.8	17.6 ± 2.9	1.5 ± .8	11.2 ± 2.3
(1.9)	86	62.8 ± 8.5	25.6 ± 5.5	2.3 ± 1.6	9.3 ± 3.3
(2,4)	41	53.7 ± 11.4	19.5 ± 6.9	4.9 ± 3.4	22.0 ± 7.3

TABLE VI. PERCENTAGE OF EVENTS FOR EACH FINAL STATE CATEGORY OF SIX PRONGS

Position	# Events	Type				
		1	2	3	4	5
(1,4)	121	50.4 ± 6.5	33.1 ± 5.2	13.2 ± 3.3	3.3 ± 1.7	0.0
(1,9)	21	4.8 ± 4.8	38.1 ± 13.5	38.1 ± 13.5	9.5 ± 6.7	9.5 ± 6.7
(2,4)	46	30.4 ± 8.1	32.6 ± 8.4	30.4 ± 8.1	4.3 ± 3.1	2.2 ± 2.2

TABLE VII. PERCENTAGE OF EVENTS FOR EACH FINAL STATE CATEGORY OF EIGHT PRONGS

Position	# Events	Type						
		1	2	3	4	5	6	7
(1,4)	34	26.5 ± 8.8	41.2 ± 11.0	20.6 ± 7.8	11.8 ± 5.9	0.0	0.0	0.0
(2.4)	21	33.3 ± 12.6	23.8 ± 10.6	19.0 ± 9.5	19.0 ± 9.5	4.8 ± 4.8	0.0	0.0

TABLE VIII. NUMBER OF EVENTS FOR THE DISPERSION PARAMETER δ VS. FINAL STATE TOPOLOGY

δ	Number of Prongs			
	4	6	8	10
.1				
.3				
.5	1	16	3	3
.7	28	40	14	2
.9	72	38	14	3
1.1	57	25	7	
1.3	35	10		
1.5	12	2		
1.7	5			

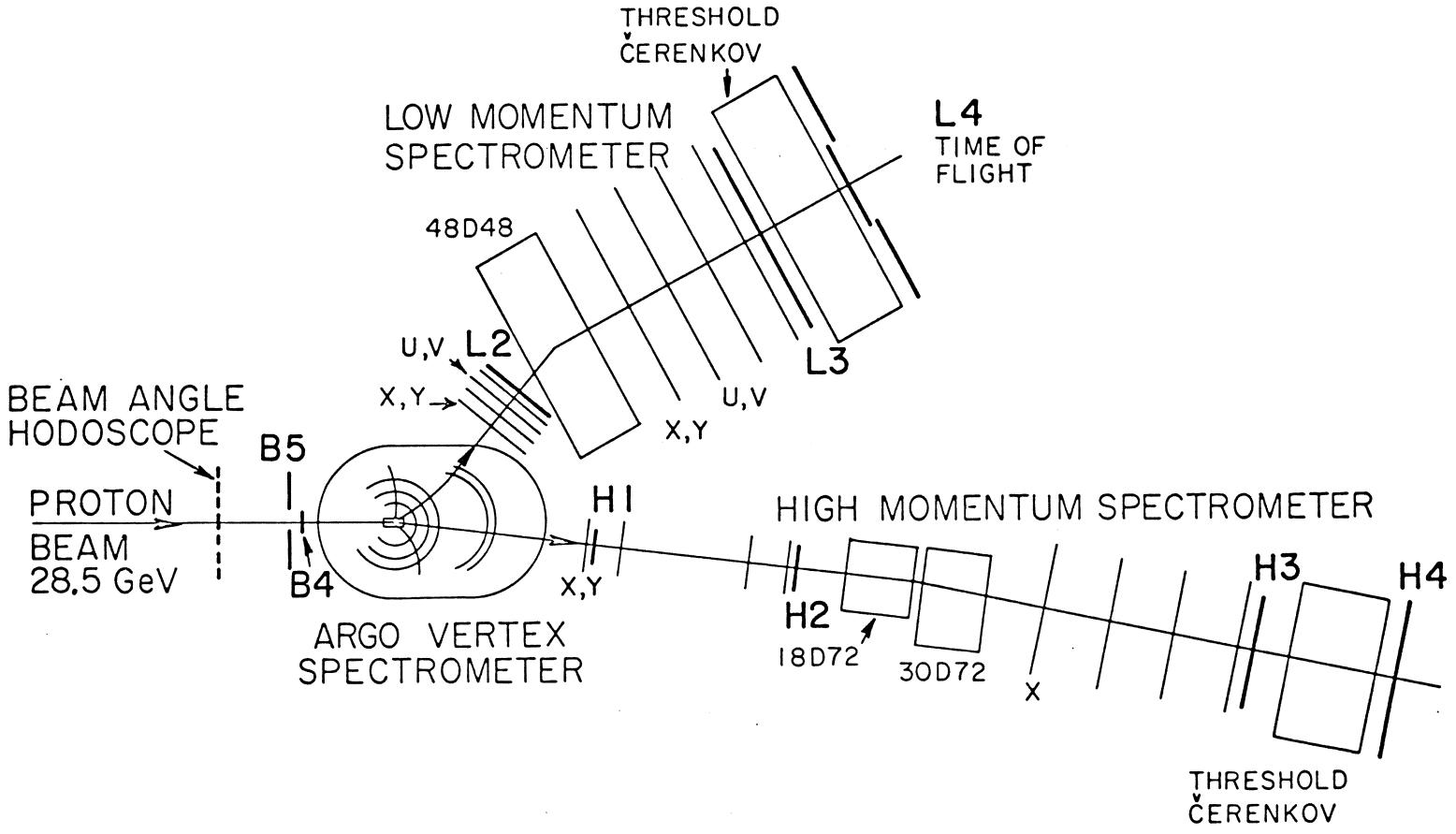

Figure 1. Schematic of the Multiparticle Argo Spectrometer System.

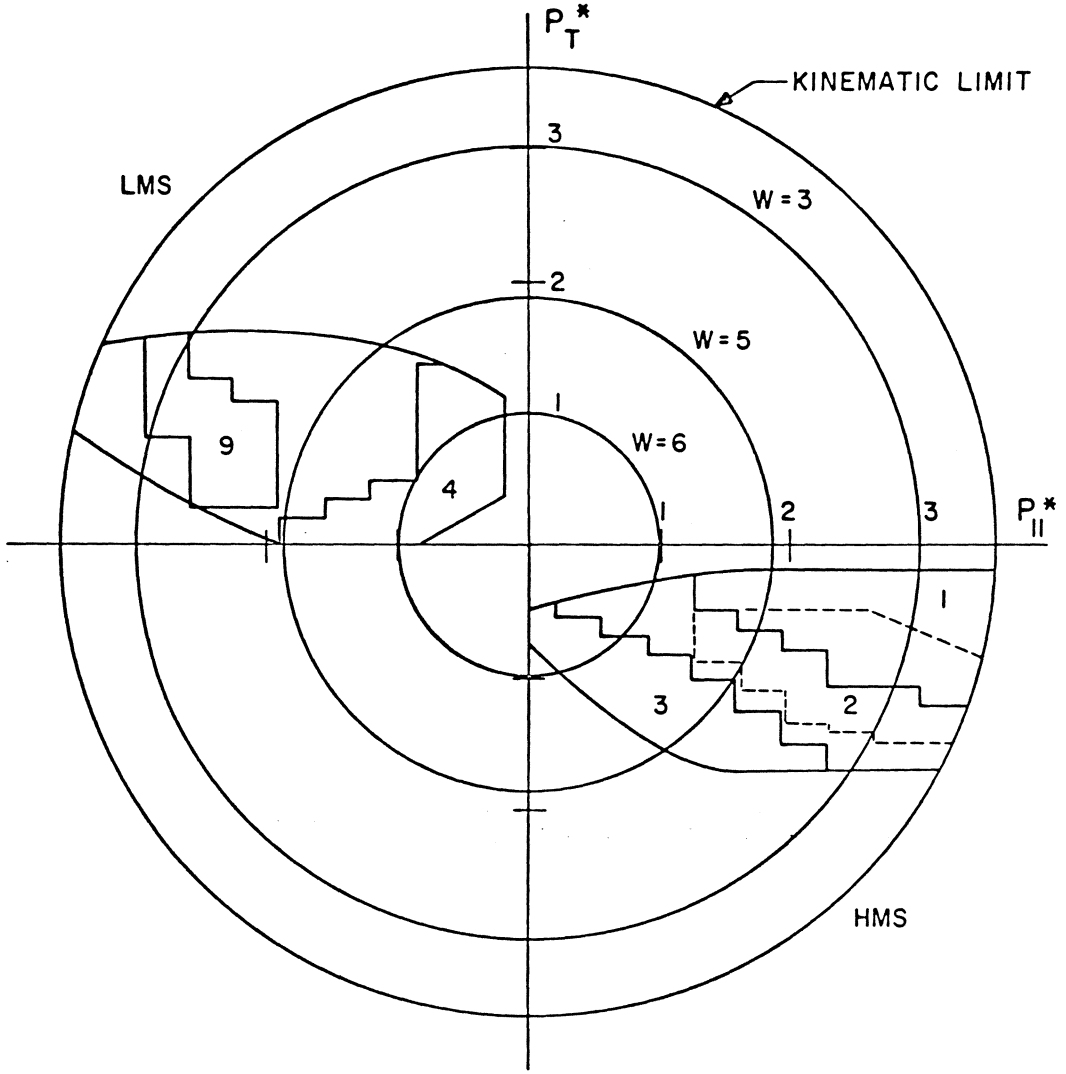

Figure 2. Phase space regions accessible to the HMS and LMS protons. The regions spanned at a few positions are outlined and numbered.

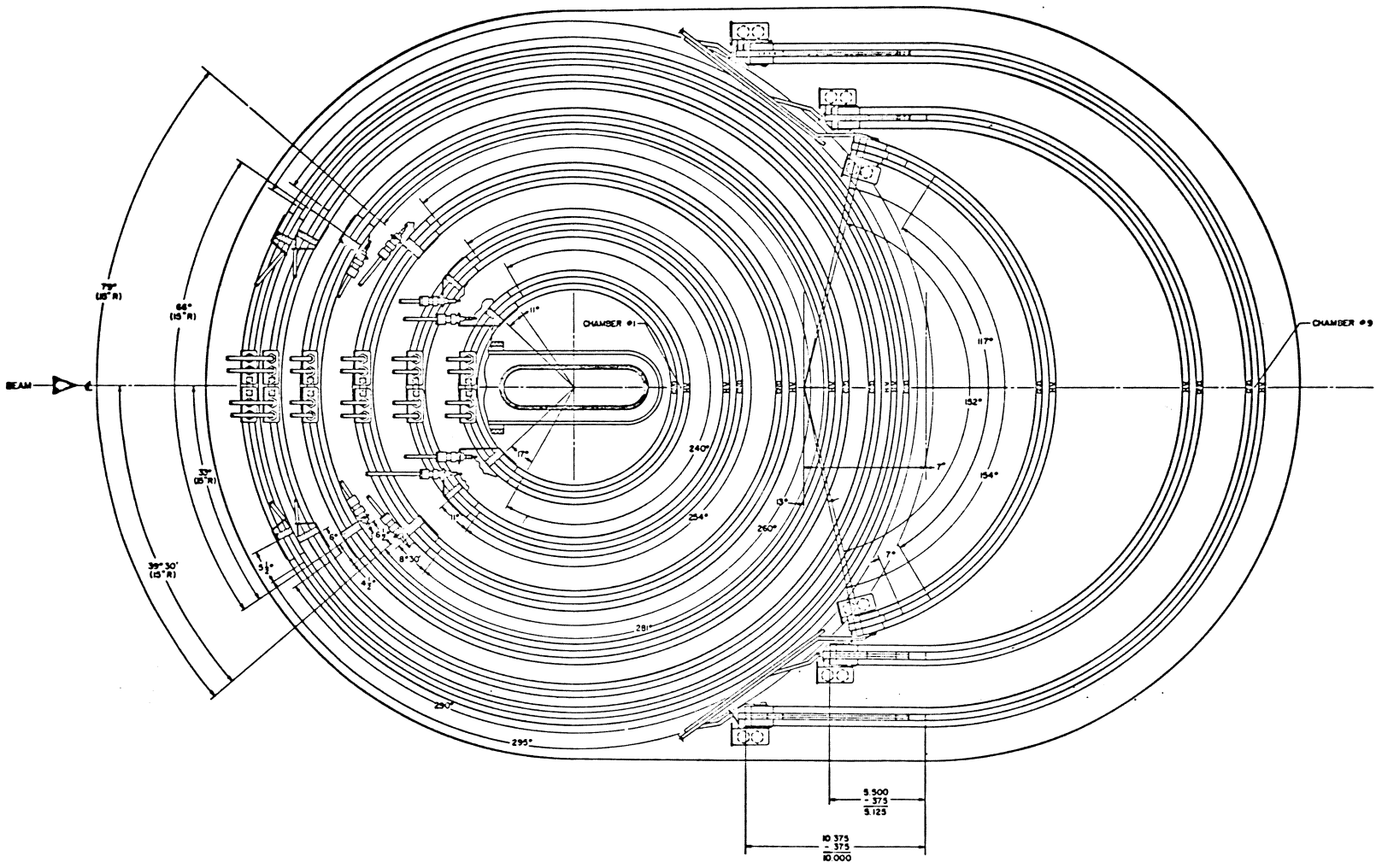

Figure 3. Schematic of the Vertex Spectrometer

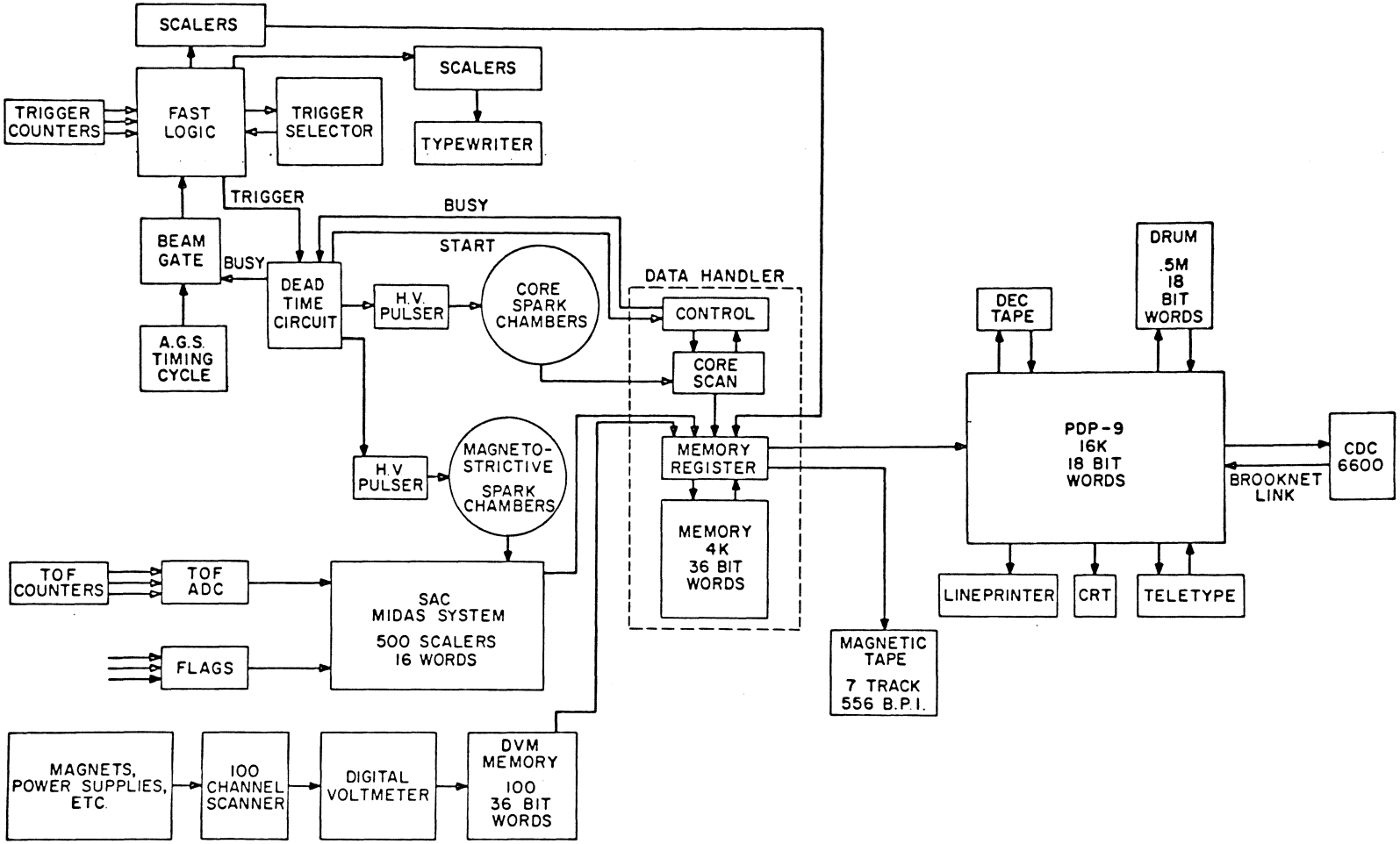

Figure 4. Data collection and storage.

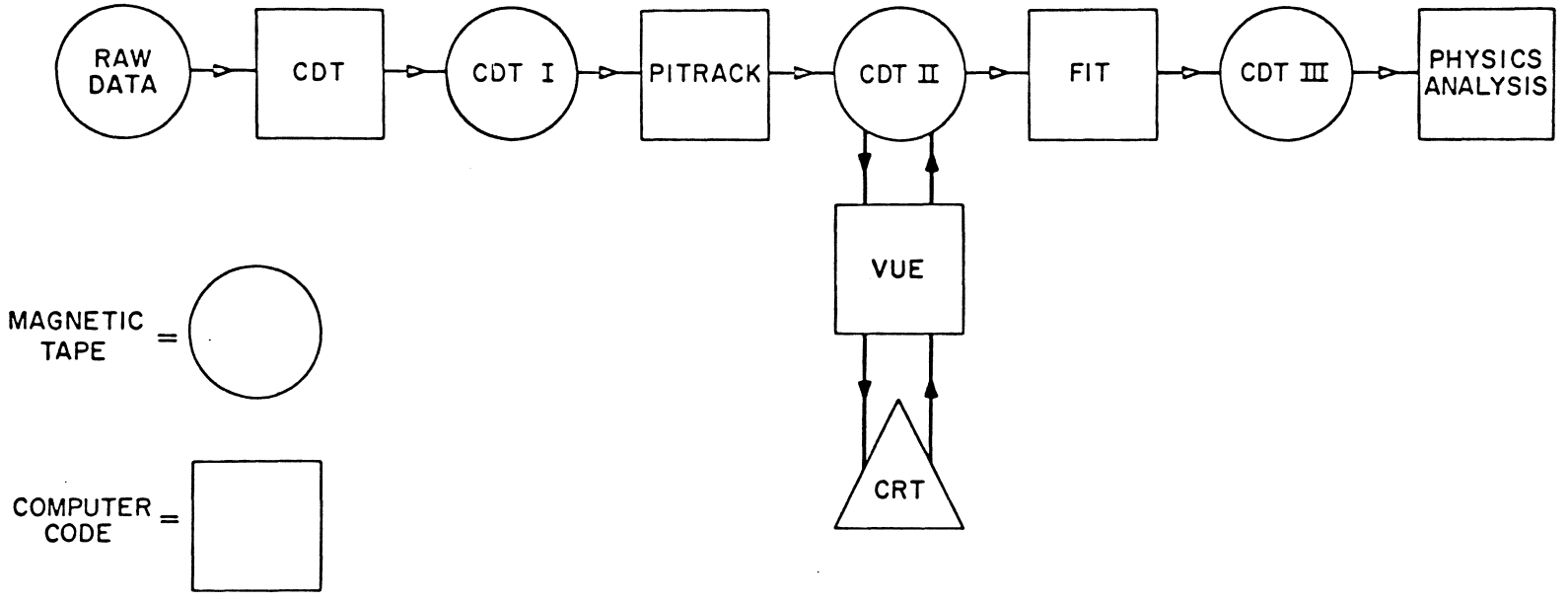

Figure 5. Computer program chain.

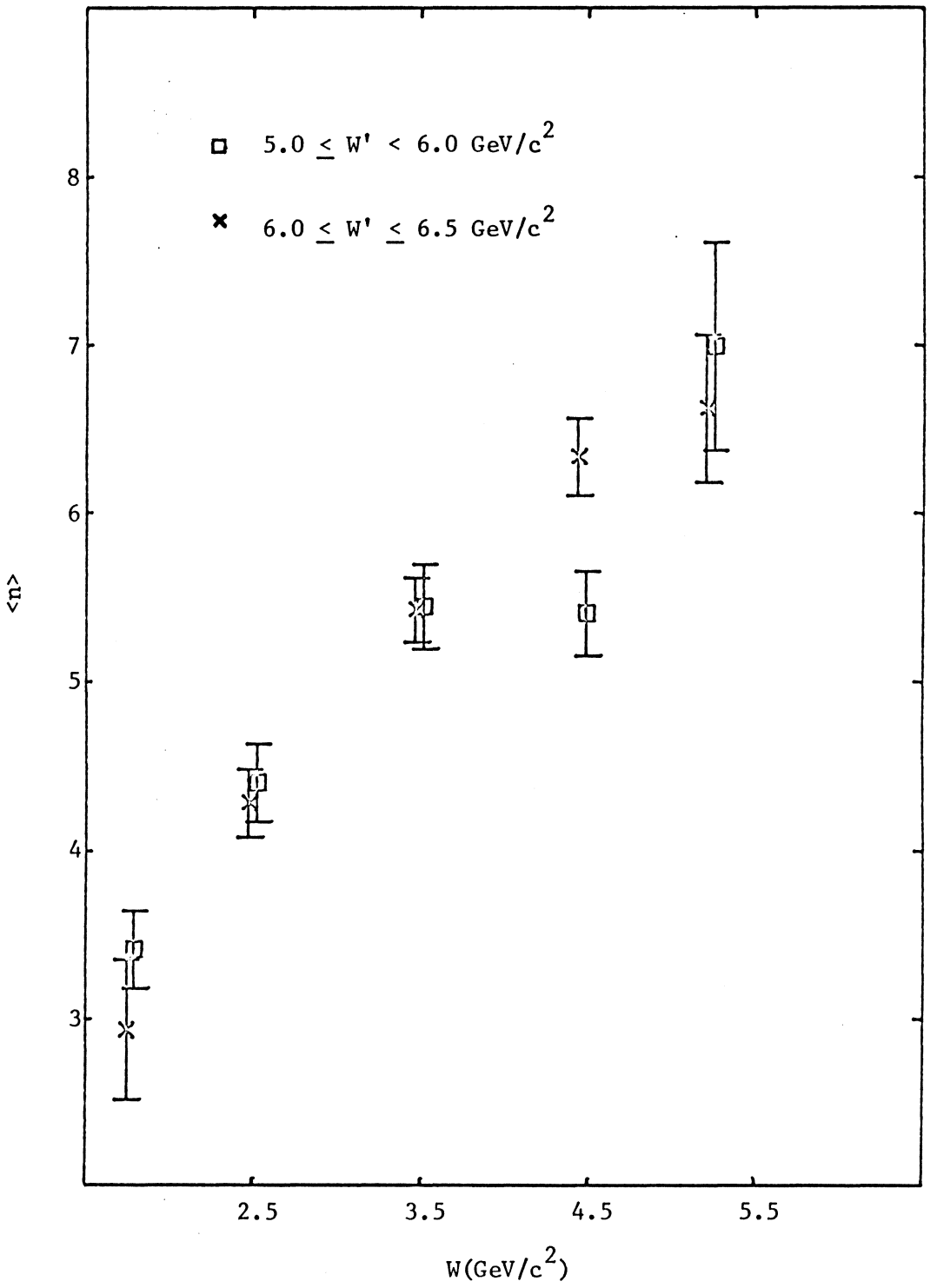

Figure 6. Average charge multiplicity vs. recoil mass for position (1,4).

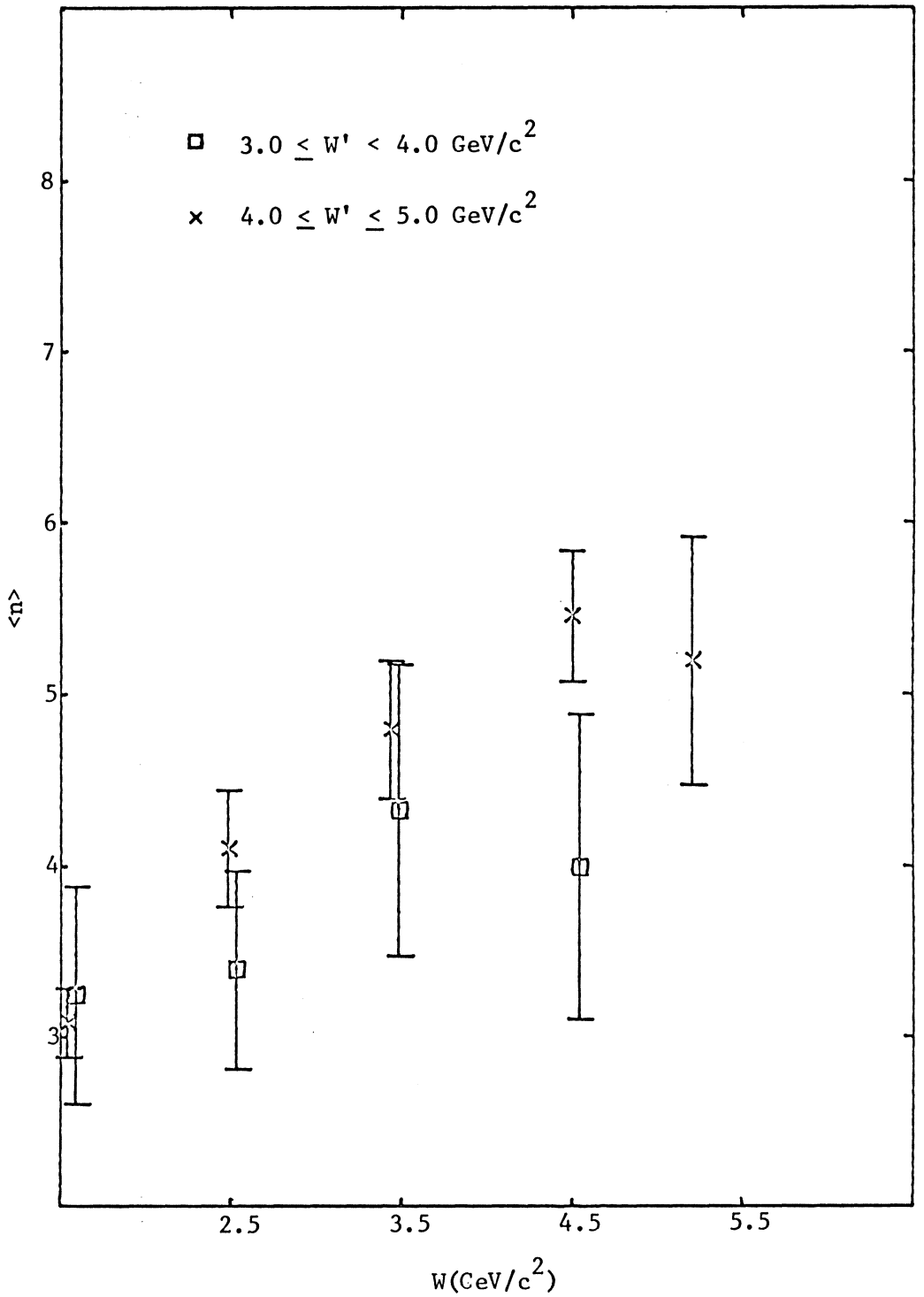

Figure 7. Average charge multiplicity vs. recoil mass for position (1,9).

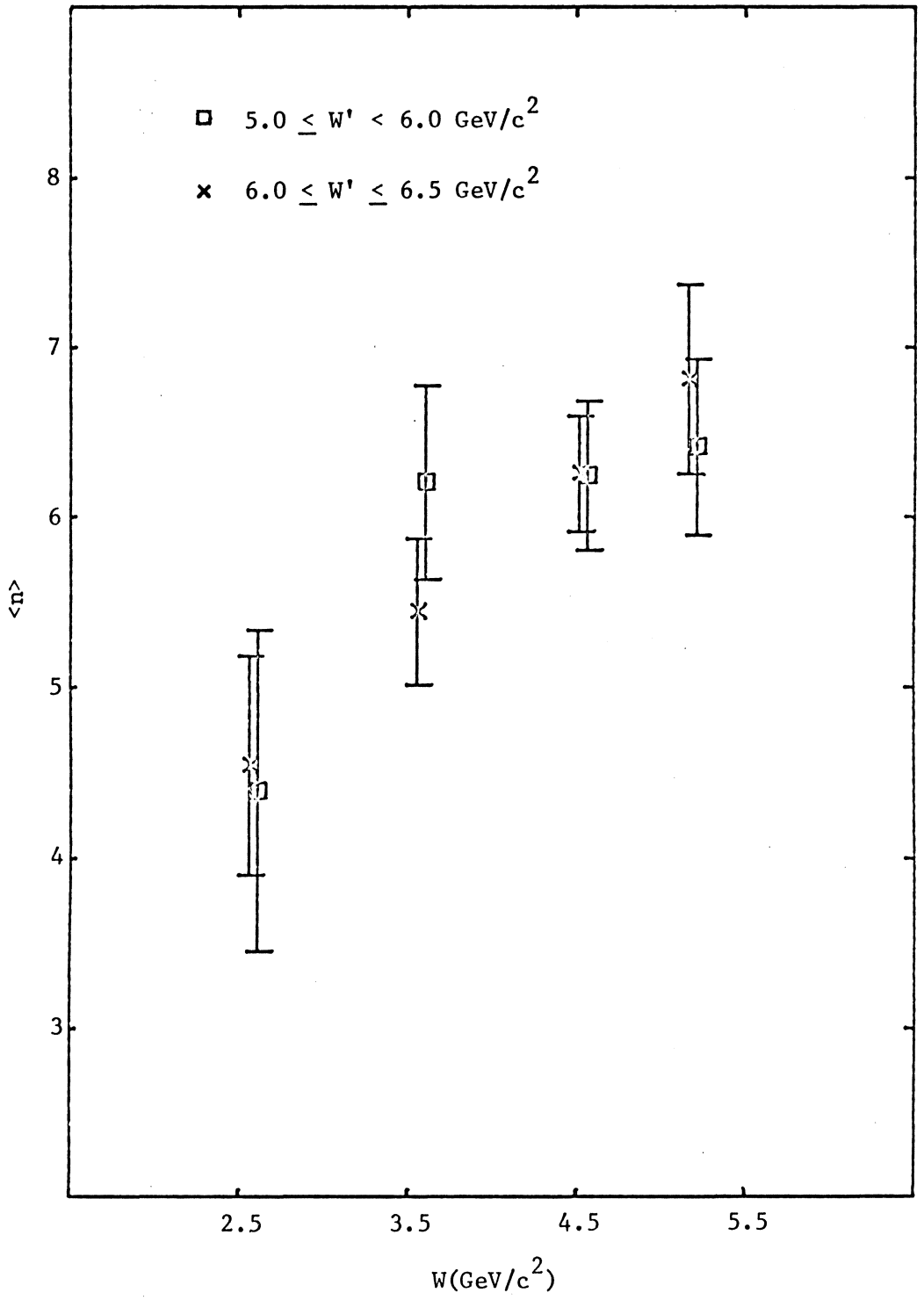

Figure 8. Average charge multiplicity vs. recoil mass for position (2,4).

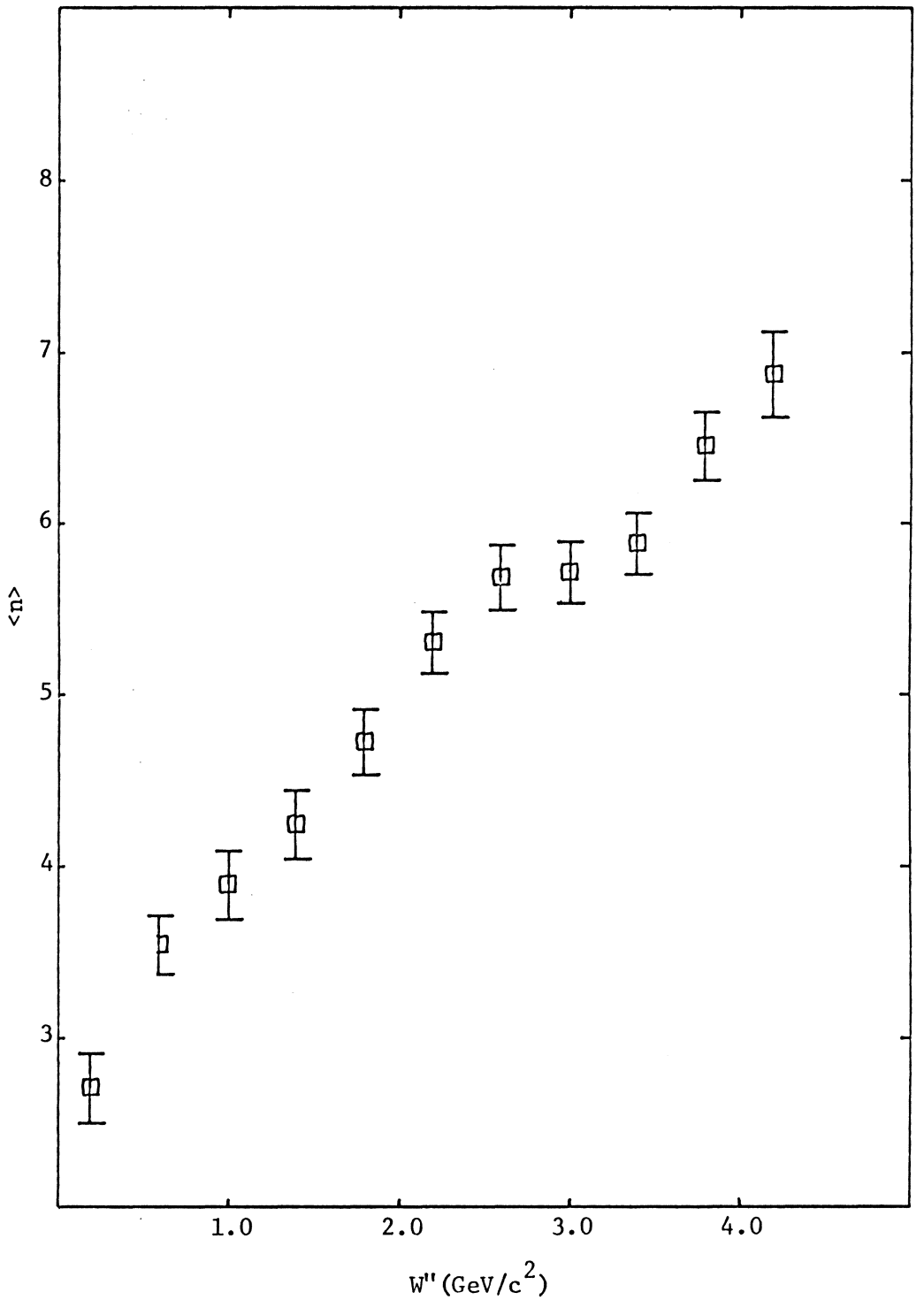

Figure 9. Average charge multiplicity vs. the double recoil mass.

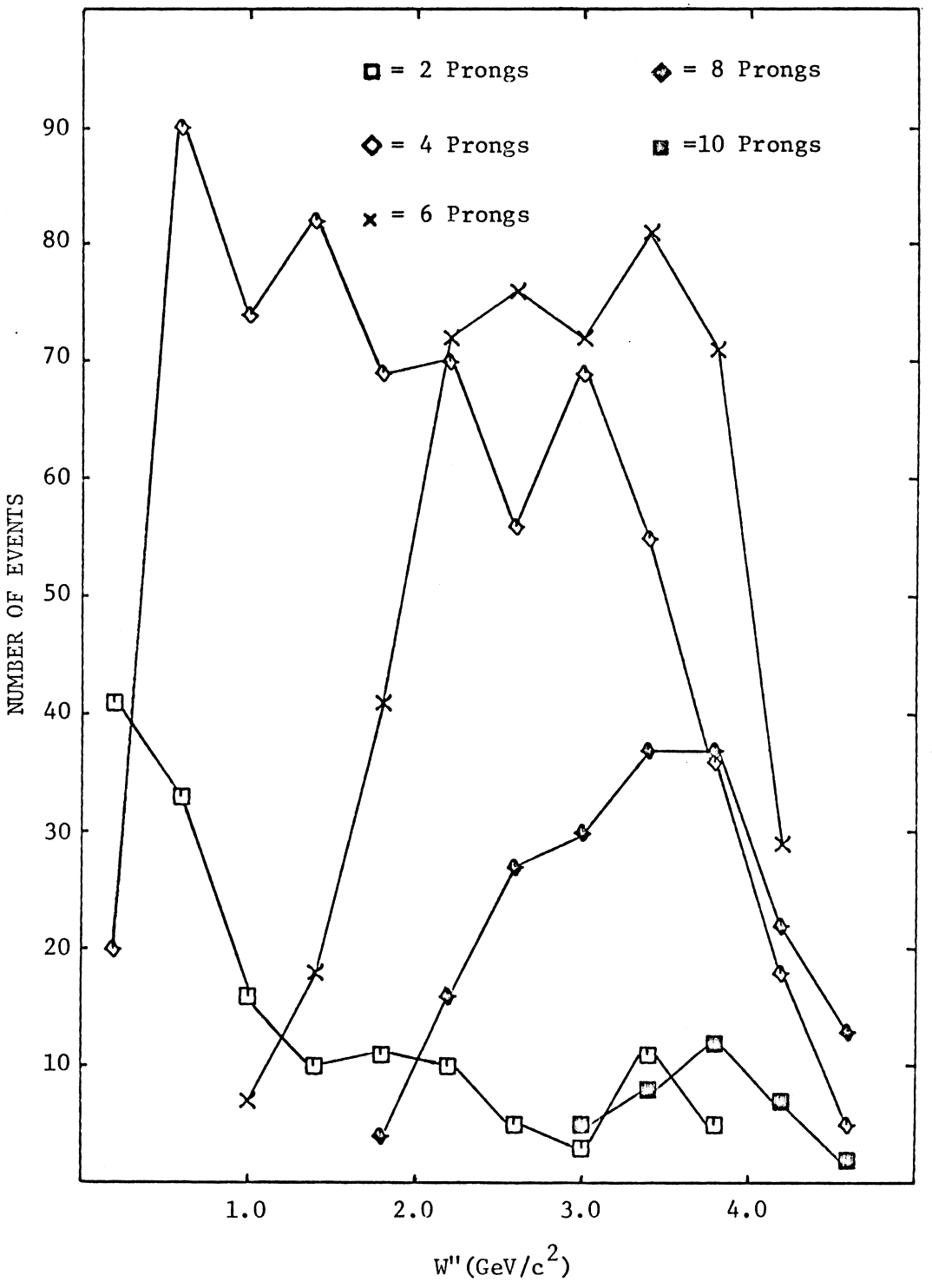

Figure 10. Number of events for each final state vs. the double recoil mass.

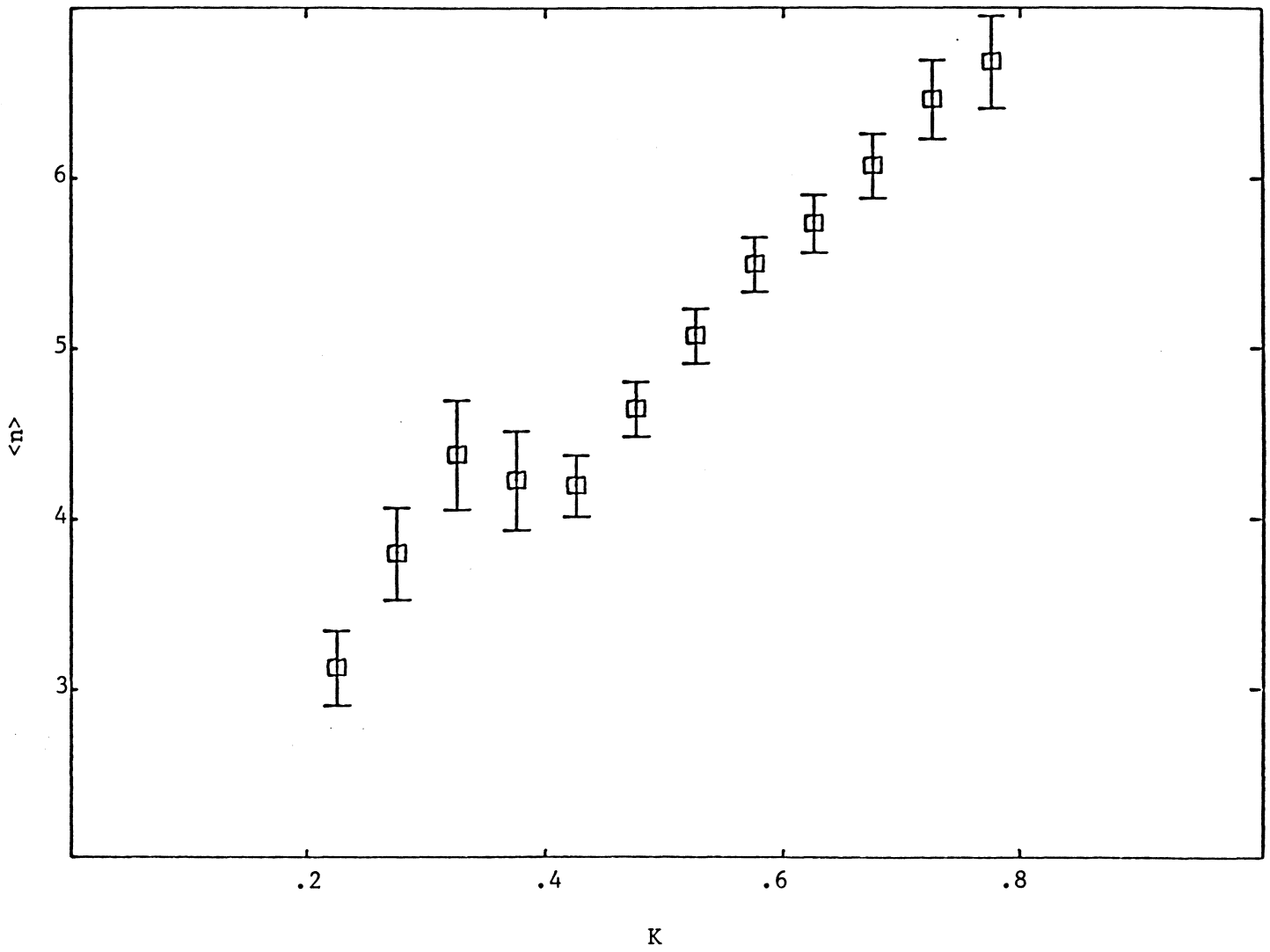

Figure 11. Average charge multiplicity vs. inelasticity.

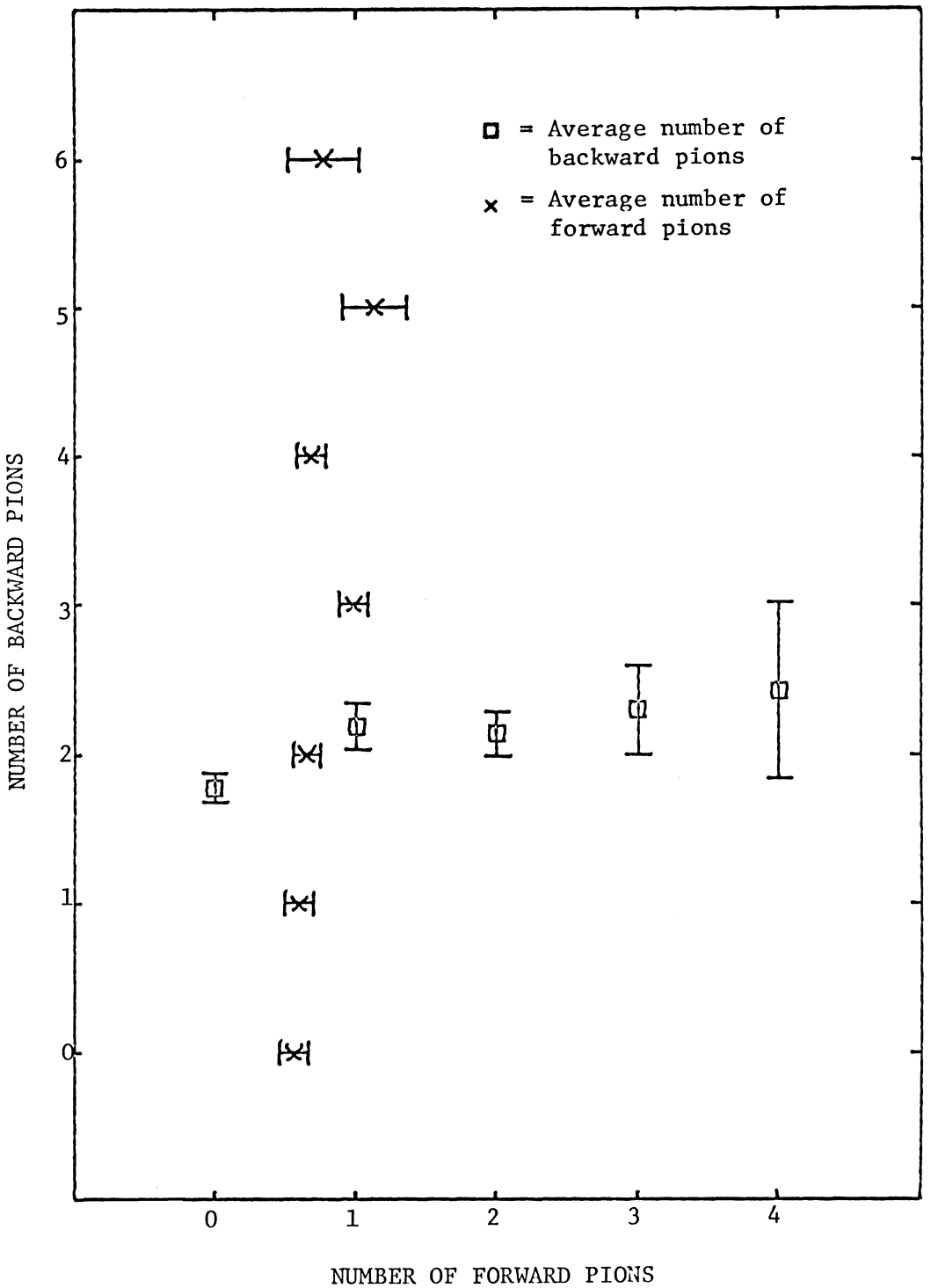

Figure 12. Number of pions backward vs. the number of pions forward in the CM for position (1,4).

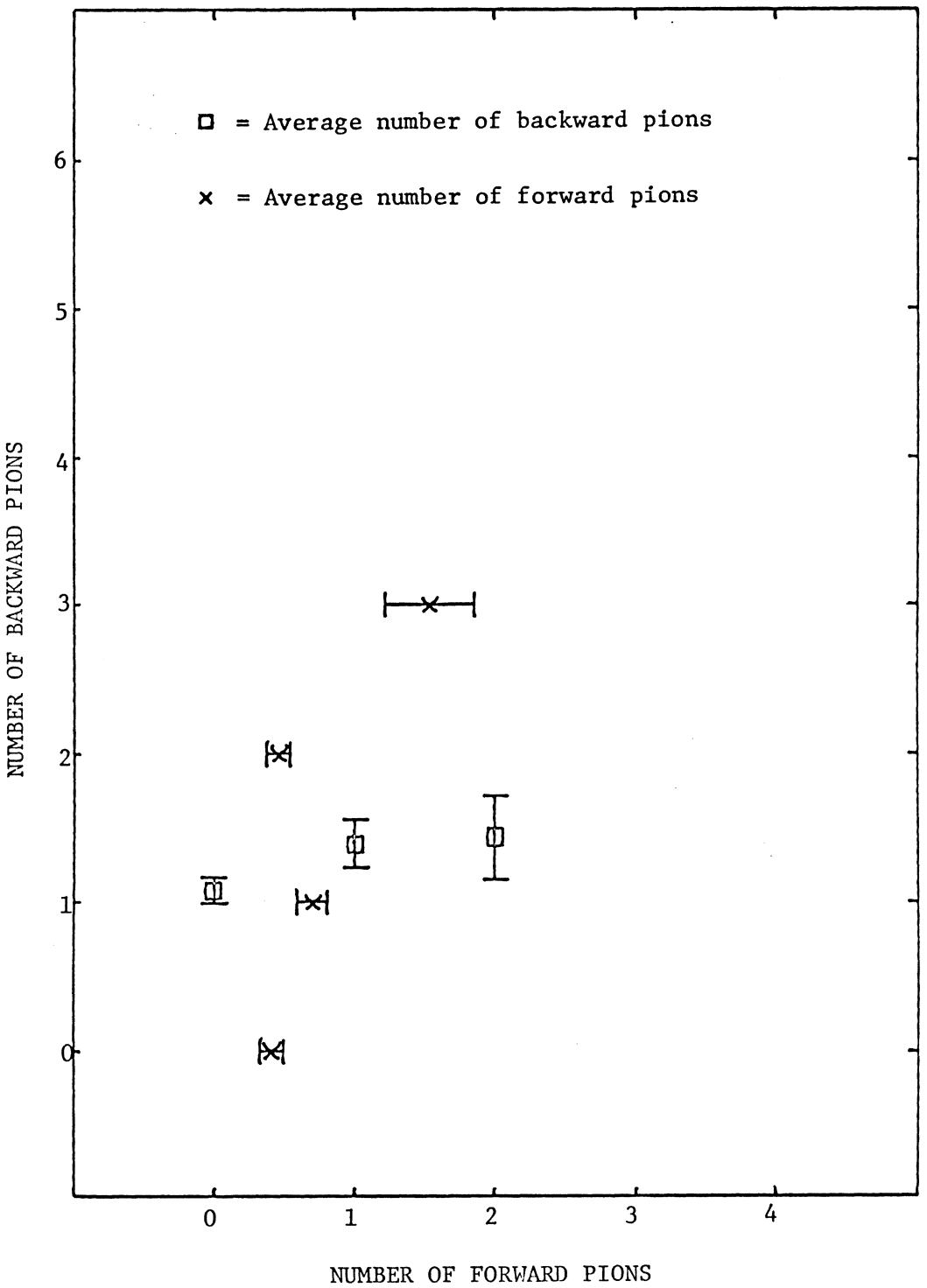

Figure 13. Number of pions backward vs. the number of pions forward in the CM for position (1,9).

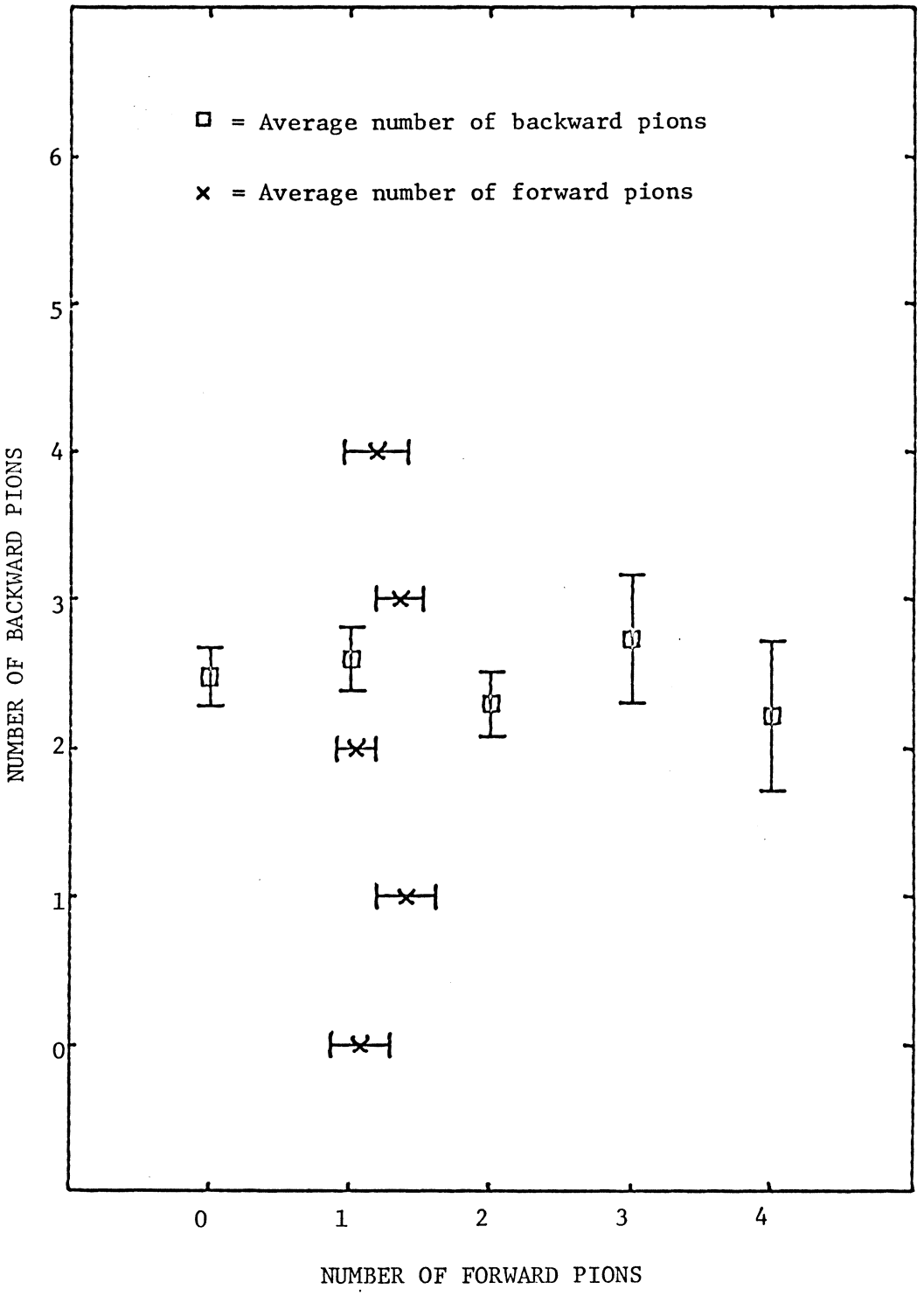

Figure 14. Number of pions backward vs. number of pions forward in the CM for position (2,4).

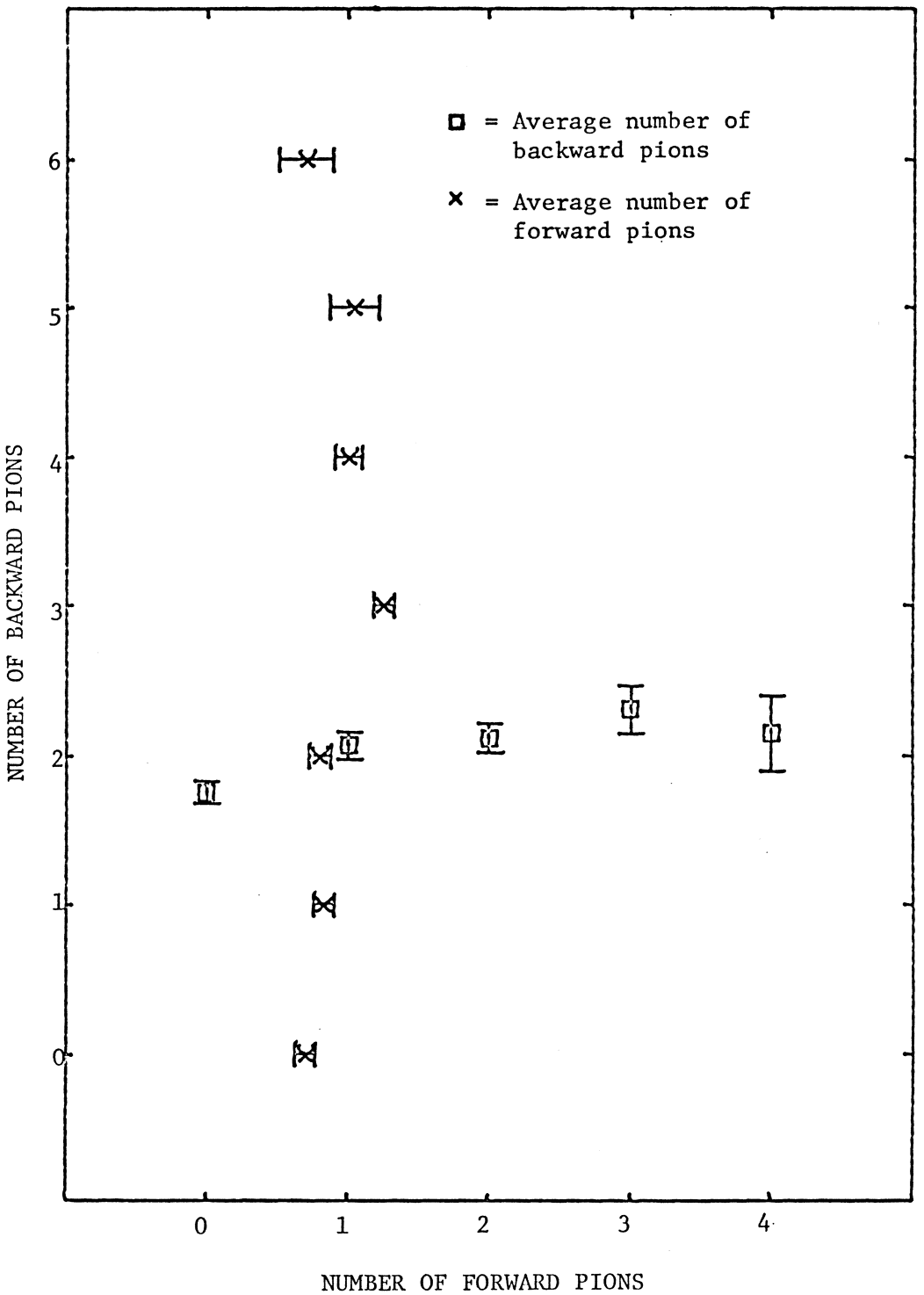

Figure 15. Number of pions backward vs. the number of pions forward in the CM for all data.

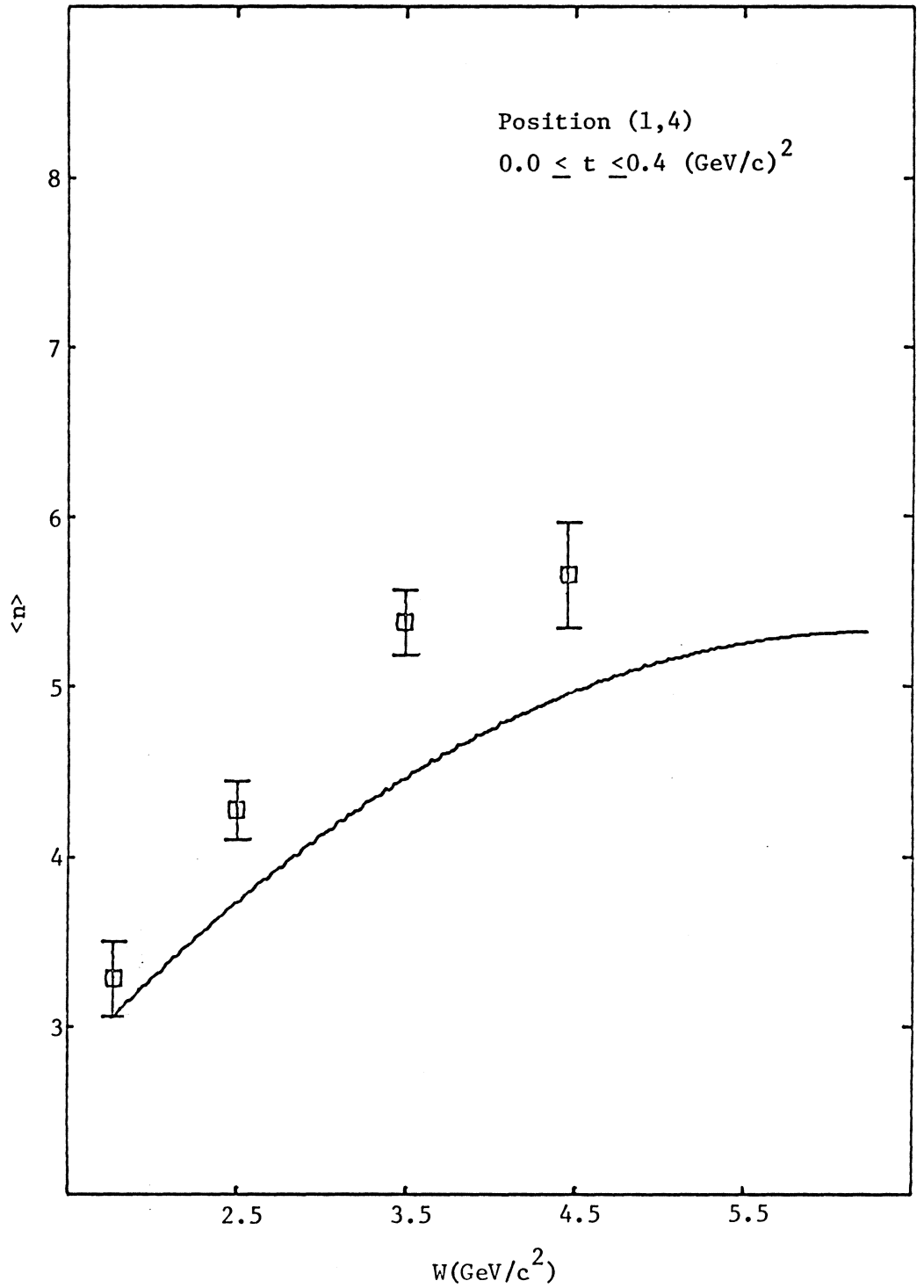

Figure 16. Average charge multiplicity vs. recoil mass for <t> = 0.2 $(GeV/c)^2$ in position (1,4). The solid line is the result from (p,-) triggers.

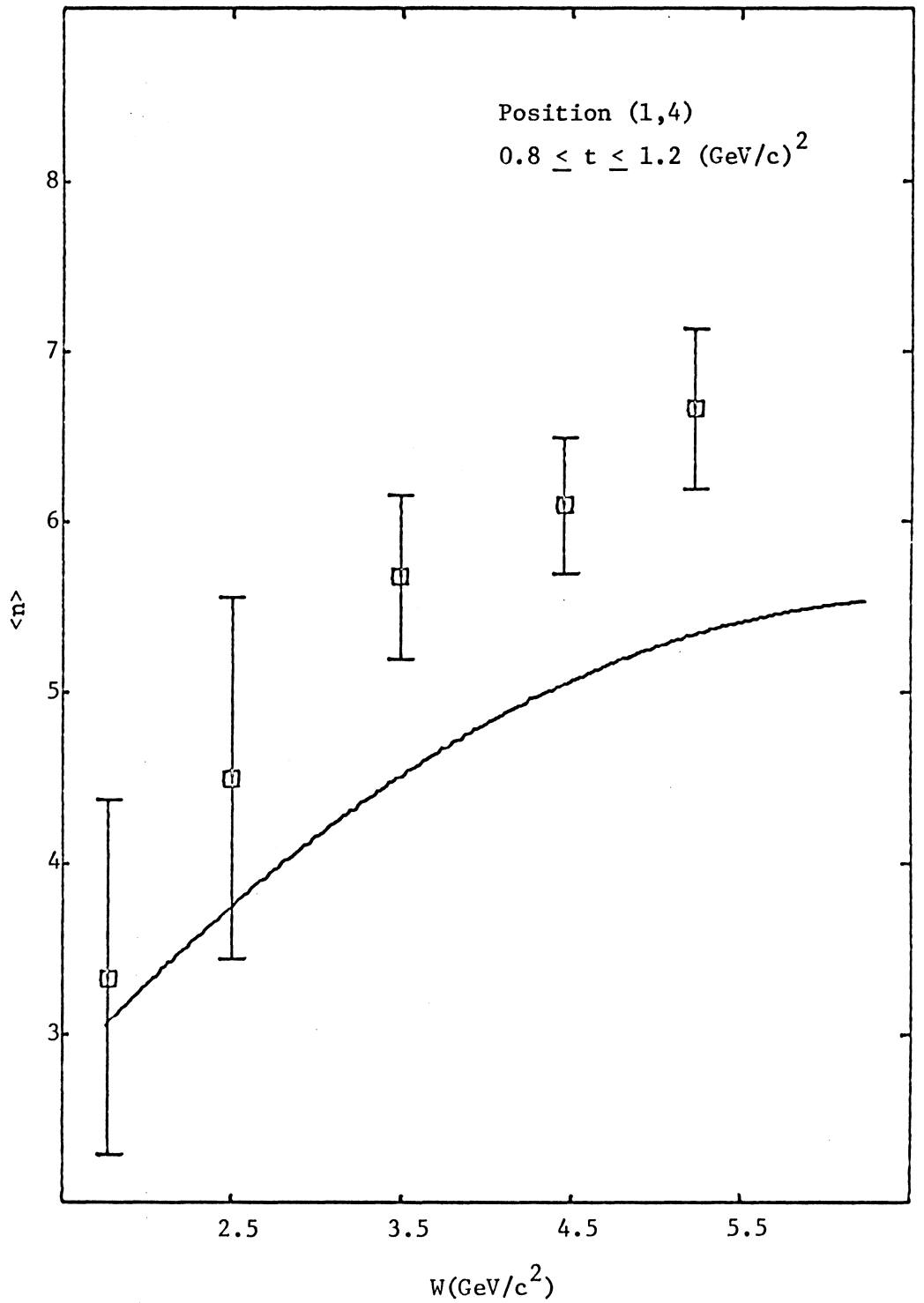

Figure 17. Average charge multiplicity vs. recoil mass for <t> = 0.9 $(GeV/c)^2$ in position (1,4).

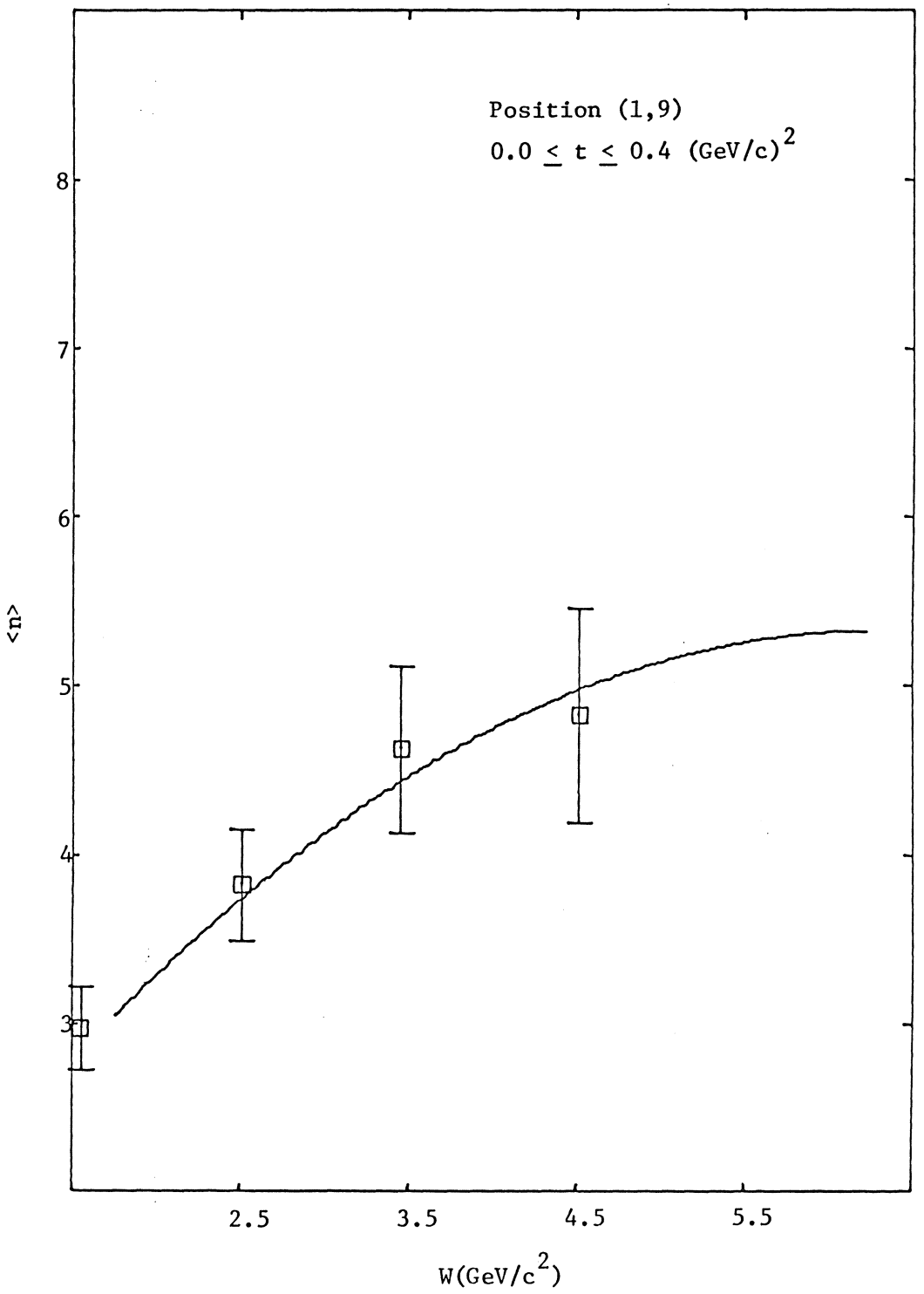

Figure 18. Average charge multiplicity vs. recoil mass for <t> = 0.3 (GeV/c)^2 in position (1,9).

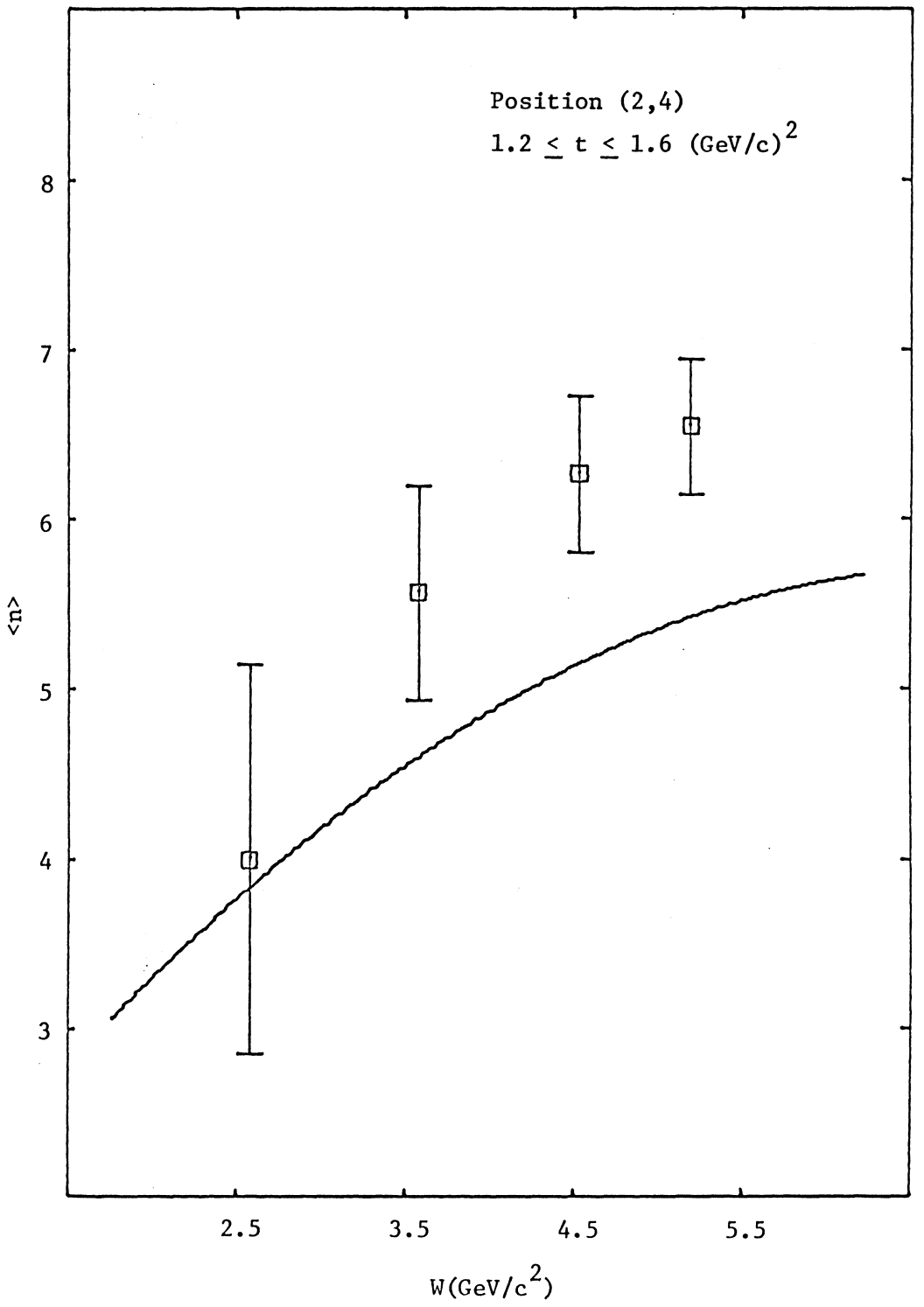

Figure 19. Average charge multiplicity vs. recoil mass for <t>=1.4 (GeV/c)^2 in position (2,4).

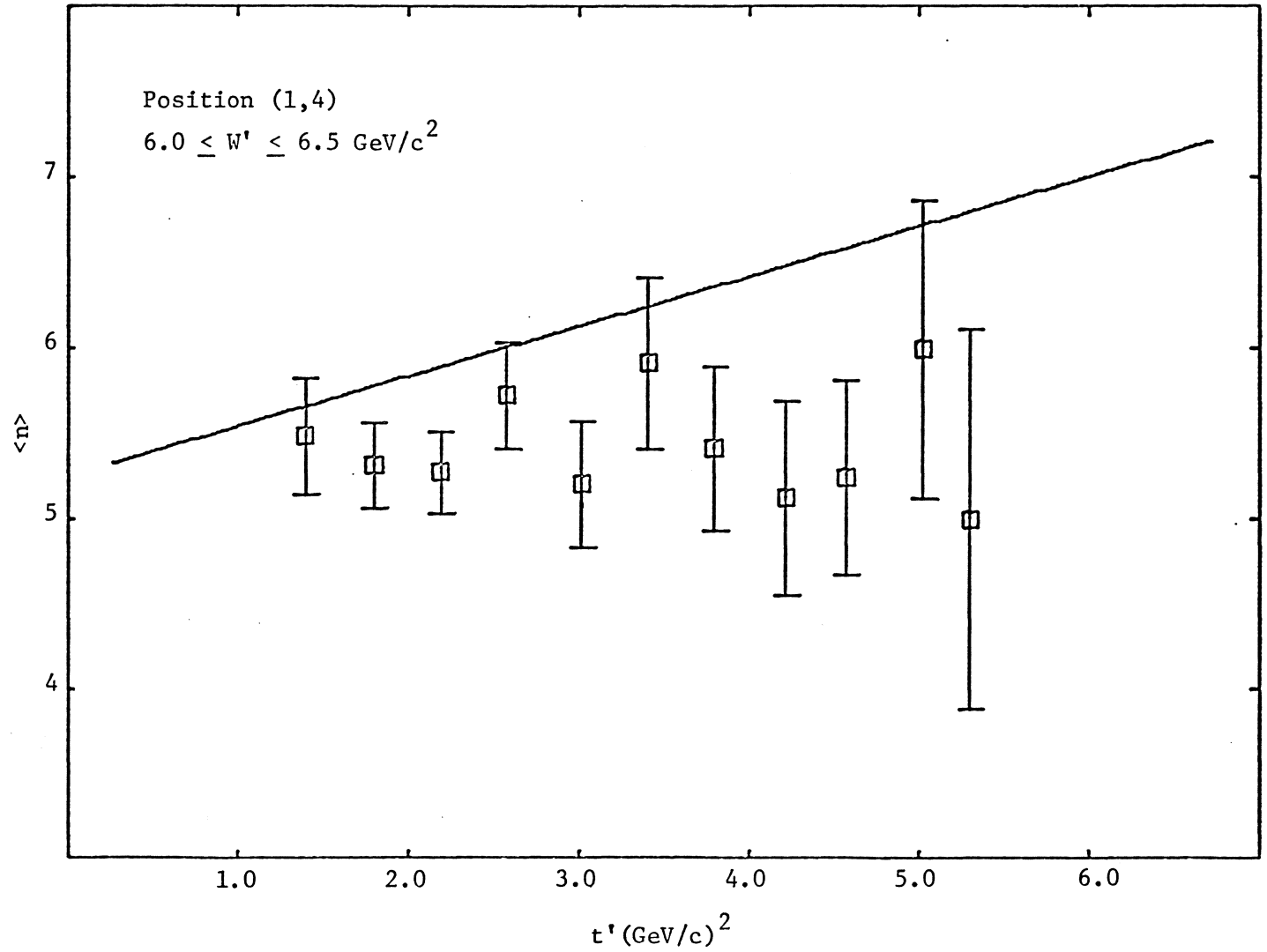

Figure 20. Average charge multiplicity vs. momentum transfer for <W'> = 6.1 GeV/c^2 in position (1,4).

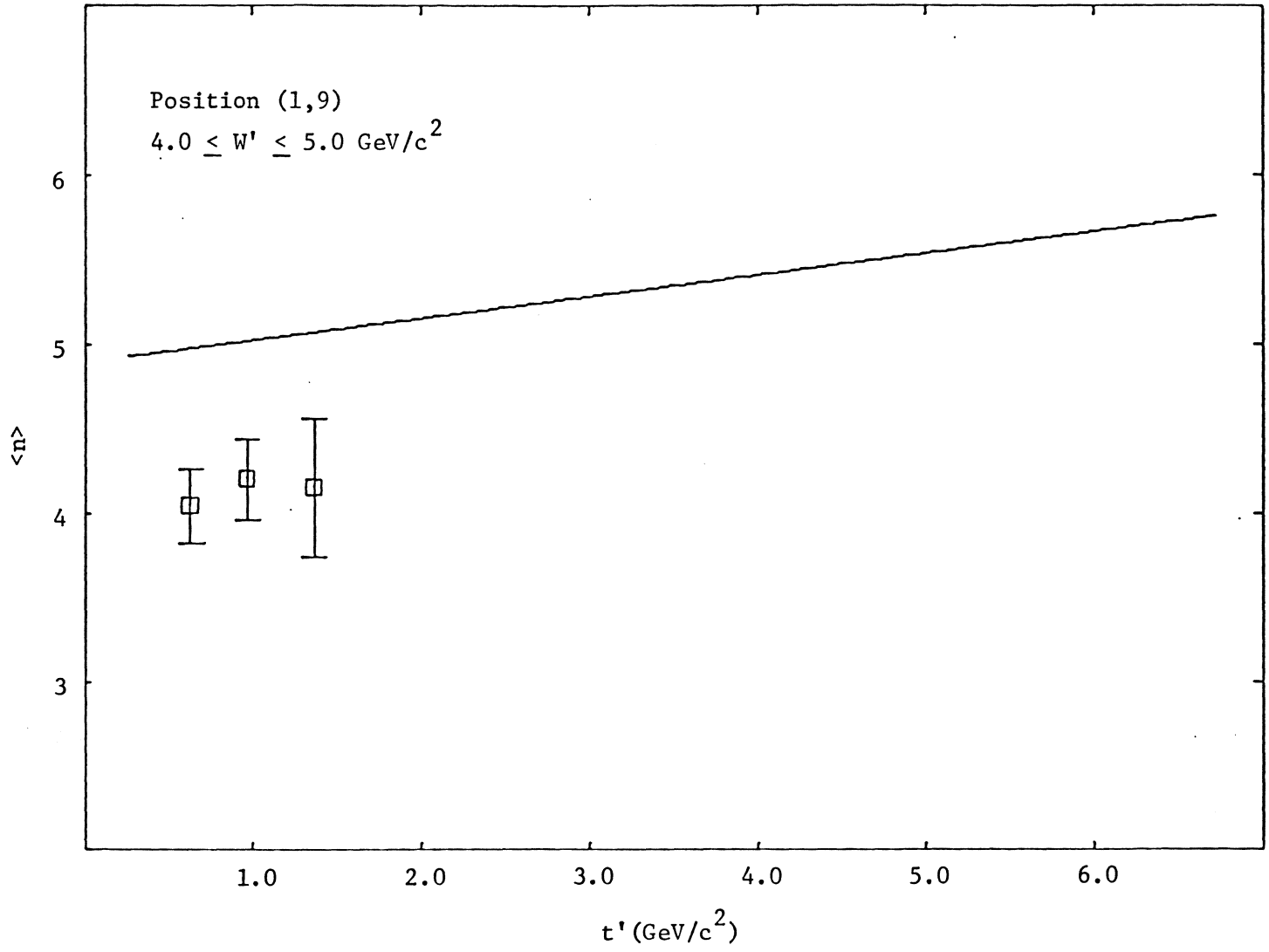

Figure 21. Average charge multiplicity vs. momentum transfer for <W'> = 4.3 GeV/c^2 in position (1,9).

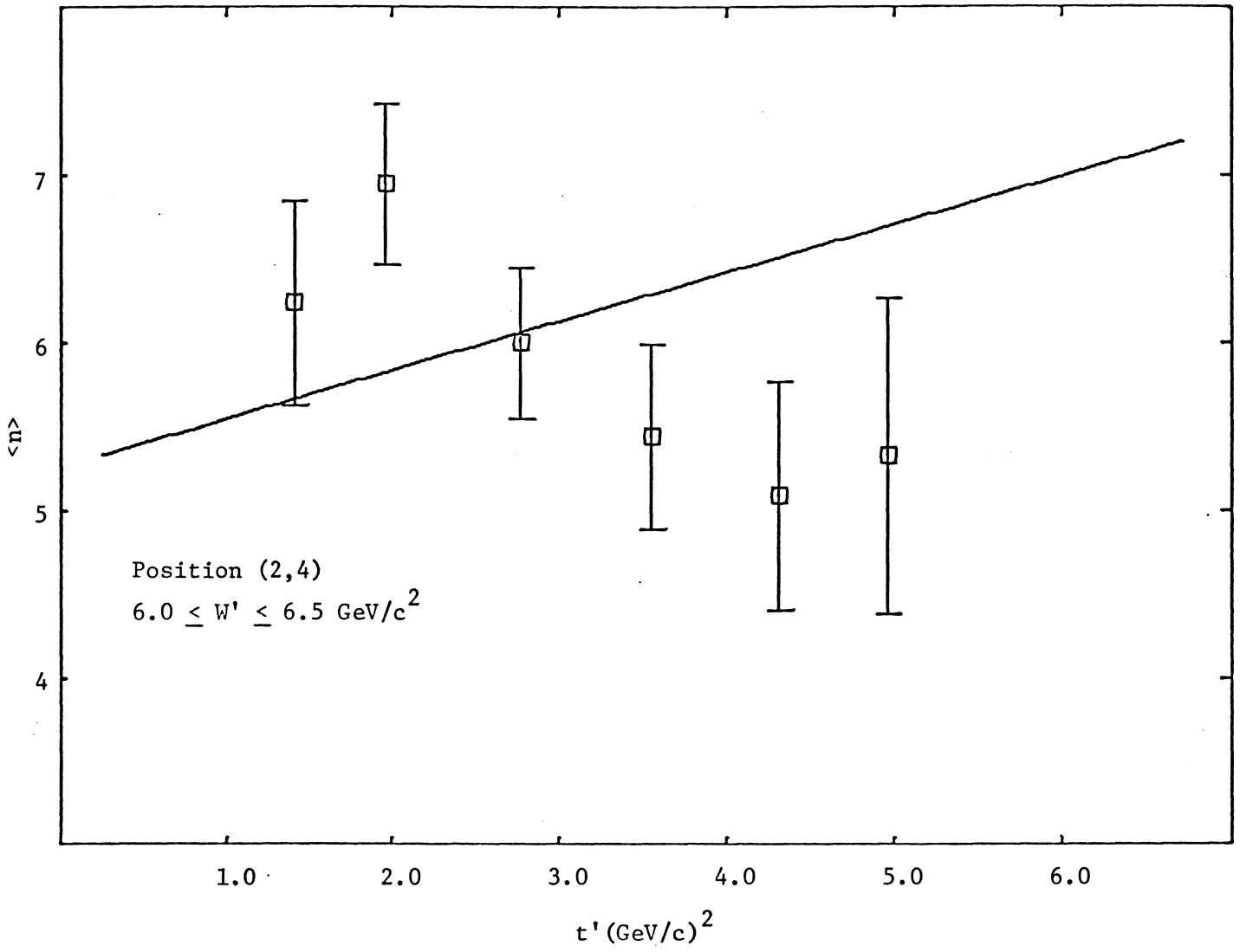

Figure 22. Average charge multiplicity vs. momentum transfer for <W'> = 6.1 GeV/c^2 in position (2,4).

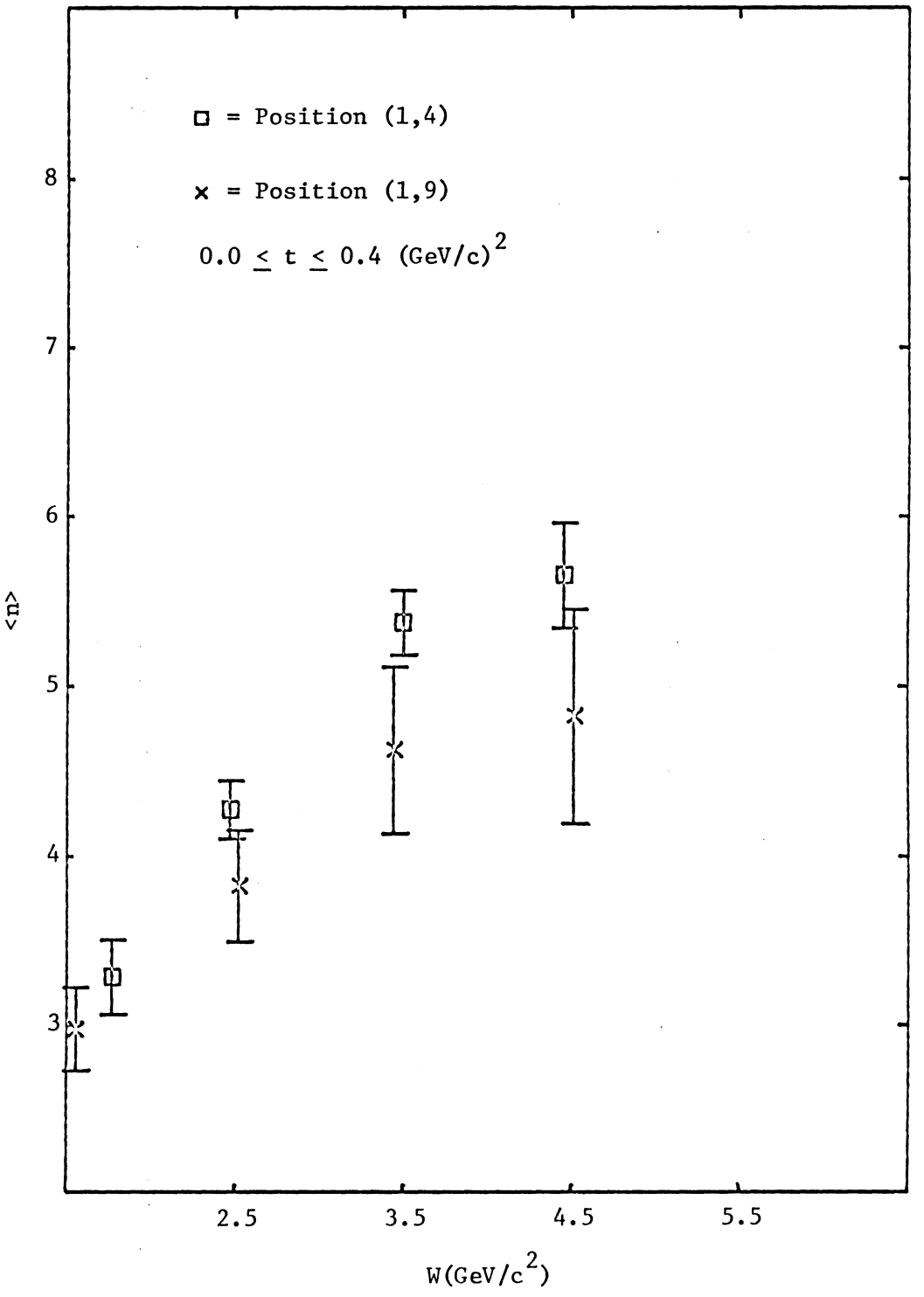

Figure 23. Average charge multiplicity vs. recoil mass for <t> = 0.2 $(GeV/c)^2$ in positions (1,4) and (1,9).

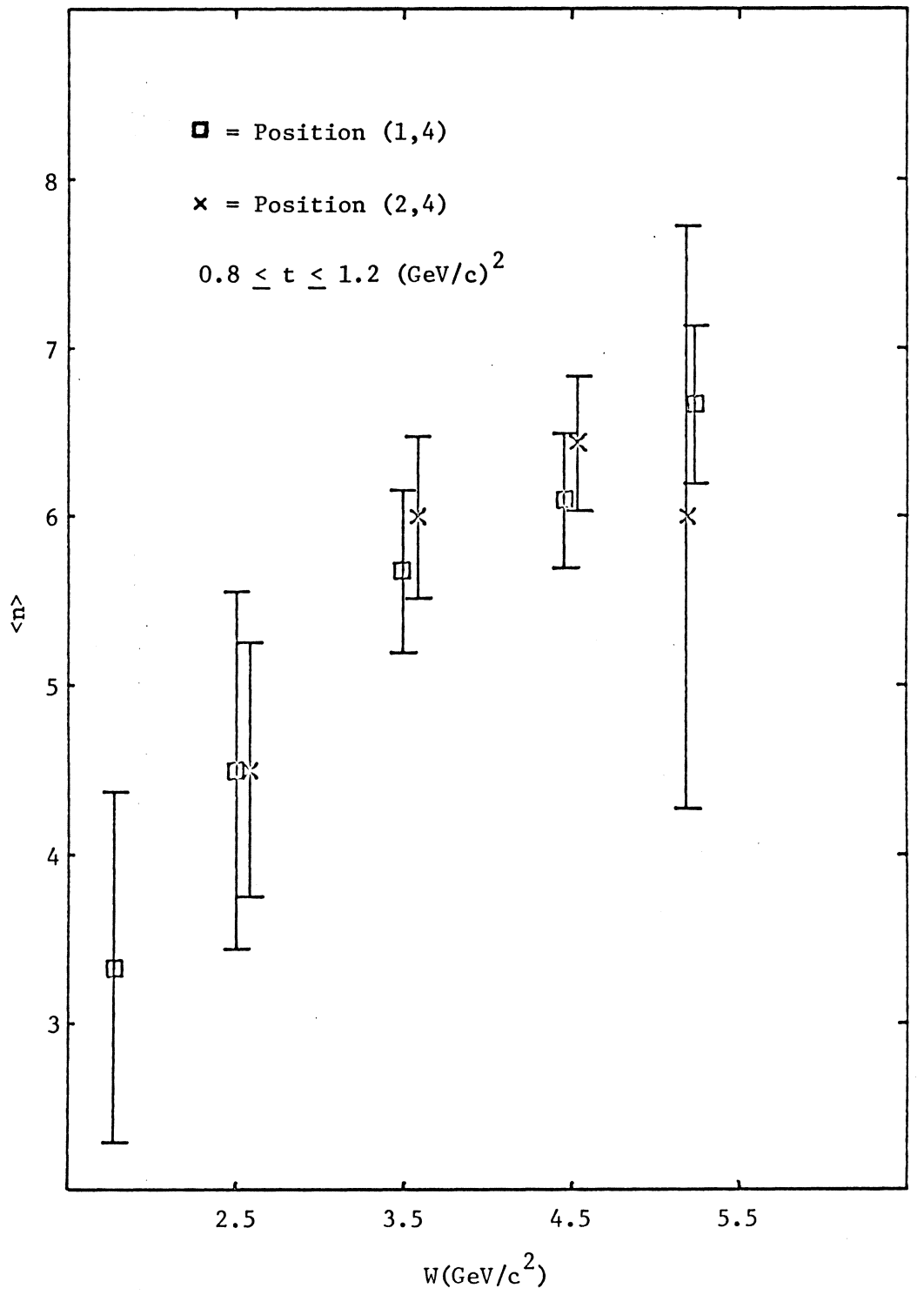

Figure 24. Average charge multiplicity vs. recoil mass for <t> = 1.0 $(GeV/c)^2$ in positions (1,4) and (2,4).

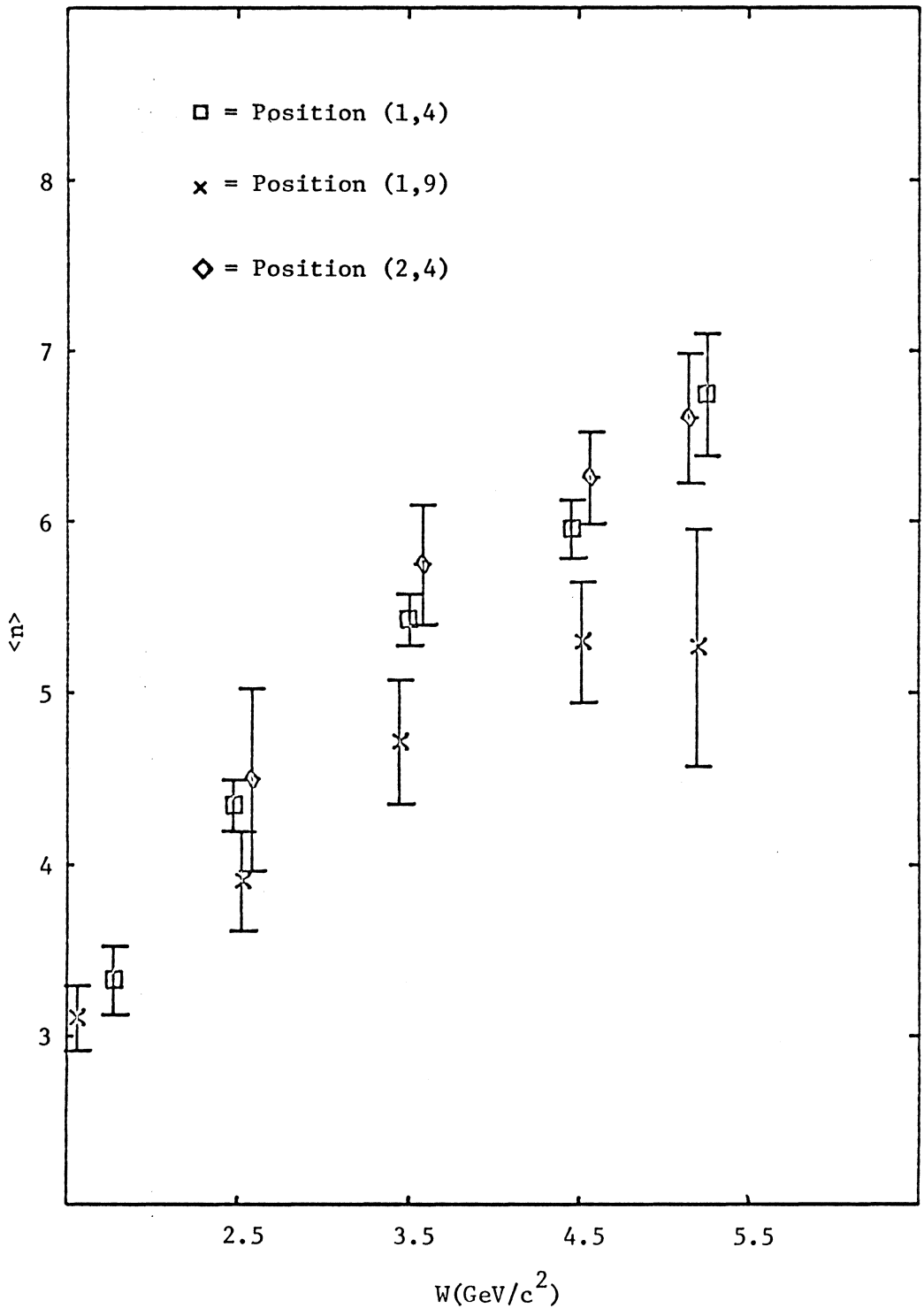

Figure 25. Average charge multiplicity vs. recoil mass for positions (1,4), (1,9) and (2,4).

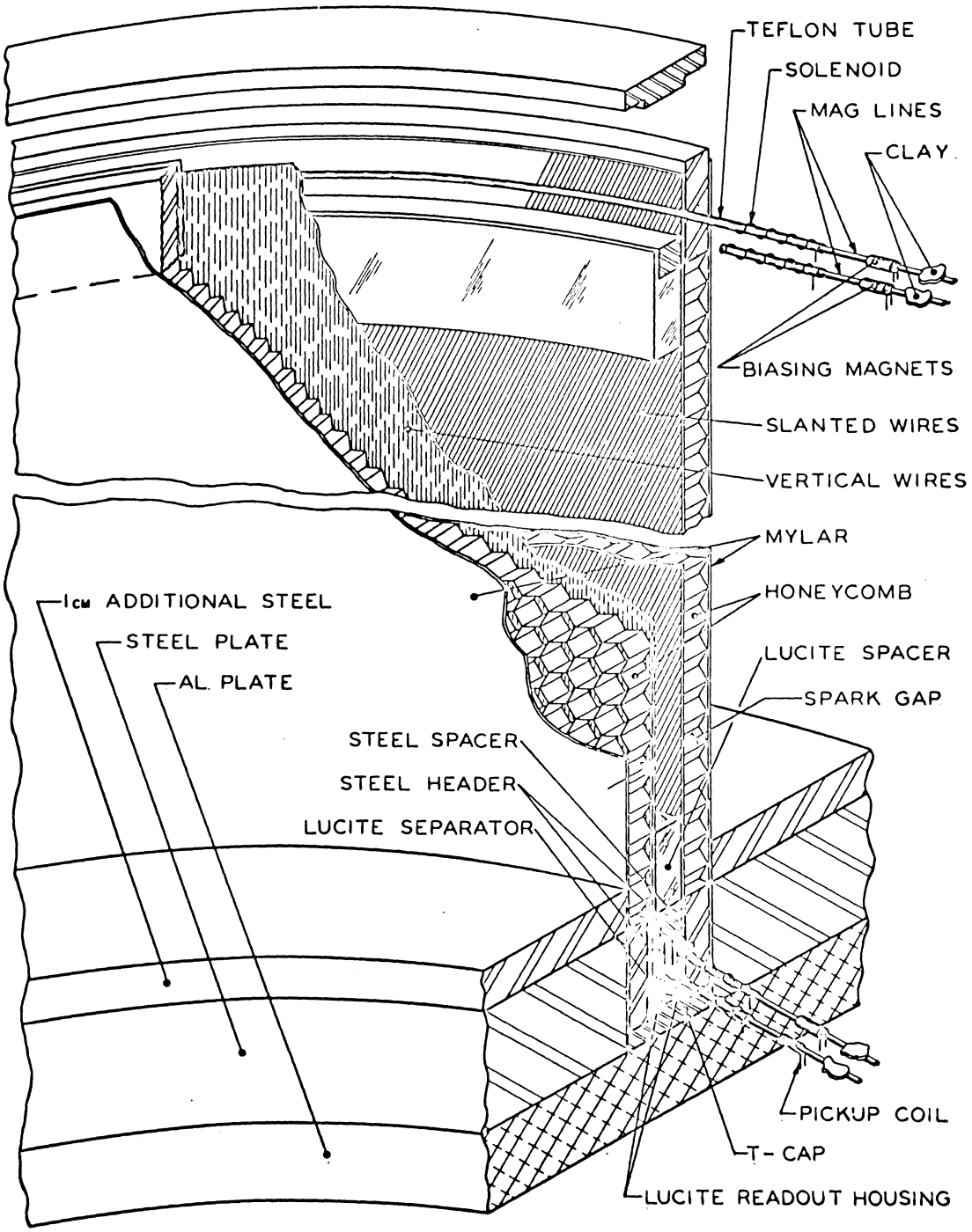

Figure 26. Schematic drawing of a cylindrical spark chamber and readout.

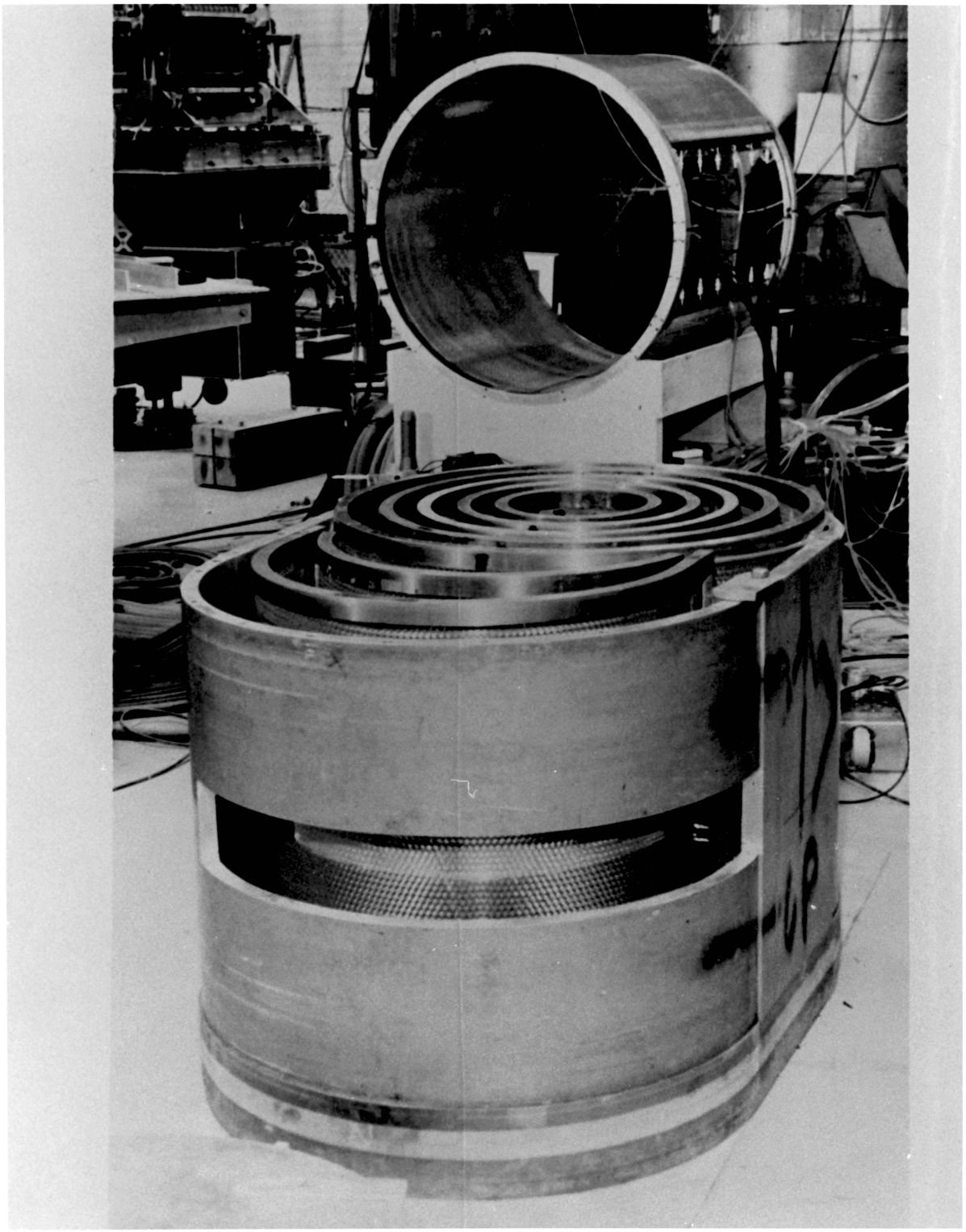

Figure 27. Spark chamber assembly with top lid removed.

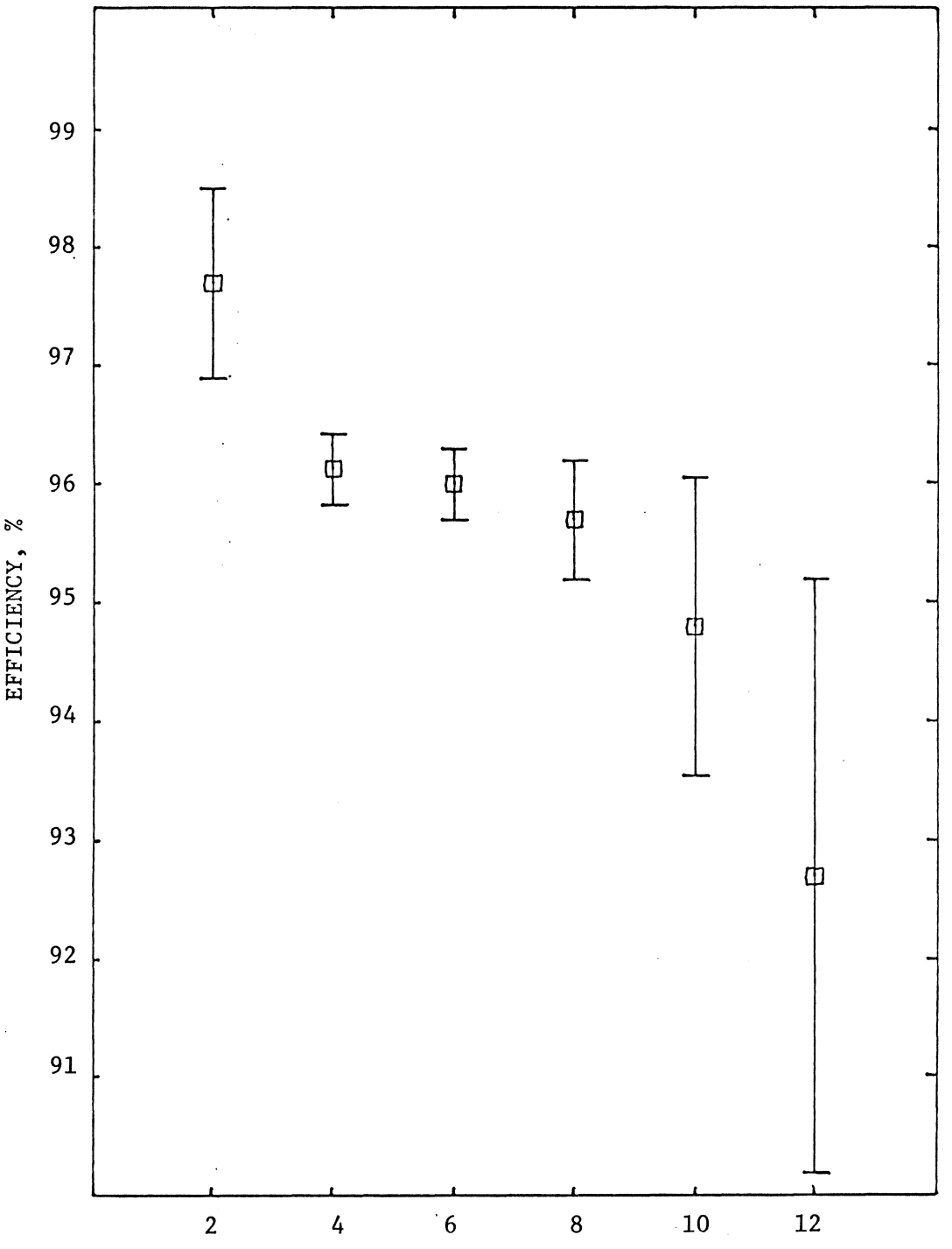

Figure 28. Spark chamber efficiency vs. multiplicity.

The vita has been removed from the scanned document

MULTIPARTICLE EVENTS WITH IDENTIFIED FINAL STATE PROTONS RESULTING FROM pp INTERACTIONS AT 28.5 GeV/c

by

Blair Culver Stringfellow

(ABSTRACT)

Using a new and unique multiparticle detection device, we have measured the average final state multiplicity for a sample of 1,500 events from the reaction $pp \rightarrow pp\ (n\pi^{\pm})$ at 28.5 GeV/c where both protons were constrained to limited regions of phase space. We find that the resulting average charge multiplicity depends linearly on the recoil mass from both protons, and on the inelasticity. A rapidity analysis indicates that low multiplicity final states are produced by one fragmenting proton, while as the multiplicity increases, so does the probability of the other proton also fragmenting. No evidence was found for multiperipheral production. We compare our data with events in which only one proton is constrained and find that the multiplicity varies with the behavior of both final state protons, the higher multiplicities occurring for more central collisions.